"Telemetering and Telecommunications Research"

NAG 5-1491: Semi-Annual Report 1993

NMSU Project Engineers:

Dr. William Osborne
Dr. Robert Paz
Dr. Michael Ross
Brian Kopp
Norm Ashley

Maneul Lujan, Jr. Space Tele-Engineering Program
Department of Electrical Engineering
New Mexico State University
Las Cruces, NM
Telephone: 505-646-3012

SECTION 1. INTRODUCTION

The NMSU Center for Space Telemetering and Telecommunications systems is engaged in advanced communications systems research. Four areas of study that are being sponsered by this grant concern investigations into the use of trellis-coded modulation (TCM). In particular, two areas concentrate on carrier synchronization research in TCM M-ary phase shift key (MPSK) systems. A third research topic is the study of interference effects on TCM, while the fourth research area is in the field of concatenated TCM systems.

Research on carrier synchronization in MPSK receiver structures has been motivated by the current interest in using 8 and 16 PSK TCM in power limited satellite channels to improve performance. NMSU has been involved in this research field since 1990 and prior to 1993 the main thrust of this research has concerned the theoretical analysis and simulation of MPSK carrier tracking. The carrier tracking approach that has been studied (and which is used in many BPSK and QPSK satellite receivers) is the high signal-to-noise ratio (SNR) approximation to the maximum a posteriori (MAP) solution to carrier phase estimation. The optimal MAP solution is a complicated mathematical calculation and was previously considered difficult to implement. With the advent of digital receiver designs this implementation barrier is now easily breached. This has motivated the NMSU Center for Space Telemetering and Telecommunications systems to fully analyze and study the optimal solution with the intent to simulate and implement it in hardware for study and evaluation at various SNR's persuant to the investigation of MPSK TCM systems. The second section of this report, "Optimal MAP estimation for MPSK carrier tracking" contains the results of this analysis which have been conducted to date.

The hardware implementation of an MPSK carrier synchronization system has been in development at the NMSU Center for two years. The design has evolved out of a desire to conform to the above mentioned industry standard BPSK and QPSK carrier synchronization approach for comparison testing while being able to implement 8 and 16 PSK carrier synchronization. As a result the high SNR approximation was used for all four modulation formats in the first implementation of the MPSK carrier synchronization system. The system is under construction and should be completed by the end of July. Testing is scheduled immediately following construction completion and should be concluded in September. Carrier phase jitter and lock threshold measurements will be conducted in this first stage of testing. It is hoped that this data will verify previously collected theoretical and simulation data. The carrier synchronizer is described in section 3 of this report, entitled "MPSK carrier tracking

hardware project". It should be noted that the hardware implementation of the MPSK carrier synchronizer and the study of the optimal solution to MAP estimation are complementary. The digital design of the carrier synchronizer makes it a simple engineering change to implement the optimal solution and should time permit this change is scheduled for later this year.

The fourth section of this report, "the effects of radio frequency interference on trellis coded modulation", concerns a simulation project. Radio frequency co-channel interference and burst interference are imparted upon a 16 state TCM system with Viterbi decoding and upon a Pragmatic TCM system. Using signal to effective interference ratios, bit error rates of the system were obtained as a performance measure. It is demonstrated that, in the presense of co-channel interference, 8 PSK TCM can achieve substantial coding gain as compared to uncoded QPSK. In the case of burst noise TCM systems perform badly. However with the help of periodic convolutional interleavers some of the losses can be recovered.

In the final section of the report, "concatenated trellis codes" research work into combining TCM with Reed-Solomon (RS) codes is discussed. Previously, combinations of RS codes with binary convolutional codes have been used to achieve 10e-10 and 10e-20 BER's. The need for more spectrally efficiency has prompted investigations into exchanging the binary convolutional inner codes with Ungerboeck codes or the recently introduced pragmatic standard. This report describes simulation work and analysis being conducted to evaluate how well these concatenated systems perform.

SECTION 2. OPTIMAL MAP ESTIMATION FOR MPSK CARRIER TRACKING

2.1 INTRODUCTION

Technological advances continue to push the limits of the state-of-the-art in all areas. The area of communication systems is no different. As the demands of the "information age" require the transmission of greater amounts of data, the supply of resources is not necessarily able to keep up. This requires a more efficient use of the current facilities including satellites, transmission and reception stations, and existing equipment.

Many current communication schemes use either binary phase-shift keying (BPSK) or quaternary phase-shift keying (QPSK) schemes for data transmission. While these have proven quite effective, the question naturally arises as to the possibility of increasing the data rate by applying higher-order phase-shift keying. Thus, an understanding of the higher-order phase-shift keying is essential in answering this question.

The theory of Maximum A-Posteriori (MAP) estimation was developed in the '60s and '70s.* At that time the implementation of the optimal estimators was not possible. As a result, simplifications were considered that facilitated the use of the basic principles of the MAP estimator, while admitting an implementation with available components. Thus, the full development of the theory was not pursued. Today, due to the advances in digital technology, the implementation of the optimal MAP estimator is now tractable. We thus consider how to implement the optimal estimator in a way that will readily retrofit onto current receiver structures.

The chief result given here is a rederivation of the work of Simon* using orthonormal basis functions that are associated with the mixers and integrate-and-dump circuits found in current, industry-standard receivers. The resulting error law that is derived is a function of the in-phase and quadrature signals that arise in a Costas crossover loop.

2.2 MAP Estimation Derivation

Consider the received MPSK signal,

---

* The important works in this area are "Further Results on Optimum Receiver Structures for Digital Phase and Amplitude Modulated Signals," (1978), M.K. Simon, *Proceedings of the ICC*, pp. 42.1.1-42.1.7, and "An Optimum Phase Reference Detector for Fully Modulated Phase Shift Keyed Signals," (1969), S. Riter, *IEEE Trans.. Aero. and Elect. Systems*, Vol. AES-5, No. 4, pp. 627-631.

$$r(t) = \sqrt{\frac{2E}{T}} \cos(\omega_c t + \theta_i + \theta_m) + w(t) \tag{2.2-1}$$

where E is the signal strength, ω_c is the carrier frequency, θ_i is the phase shift in the communication channel, θ_m is the modulation angle, and $w(t)$ is additive white Gaussian noise with spectral density, N_o. It is assumed that the unknown phase shift, θ_i, is a random variable that is uniformly distributed between $-\pi$ and π radians. The receiver is thus assumed to have no prior knowledge of the channel phase shift. The receiver is to estimate θ_i by operating on the received signal $r(t)$. The criterion of optimality chosen here, under which the estimate must operate, is the maximum a-posteriori (MAP) probability criterion.

For the MPSK signal, in order to find the MAP estimator of the received channel phase, we must maximize $\rho(\theta_i|r)$ with respect to θ_i. By Bayes' Rule, we obtain

$$\sup_{\theta_i} \rho(\theta_i|r) = \max_{\theta_i \in (-\pi,\pi]} \rho(\theta_i|r) = \max_{\theta_i \in (-\pi,\pi]} \frac{\rho(r|\theta_i)\rho(\theta_i)}{\rho(r)}. \tag{2.2-2}$$

Since the natural logarithm is a continuous, monotonically increasing function of a positive argument, then maximizing (2.2-2) with respect to θ_i is equivalent to maximizing the logarithm with respect to θ_i. Thus, applying the logarithm gives

$$\max_{\theta_i \in (-\pi,\pi]} \left\{ \ln\left[\rho(\theta_i|r)\right] \right\} = \max_{\theta_i \in (-\pi,\pi]} \left\{ \ln\left[\rho(r|\theta_i)\right] + \ln(\rho(\theta_i)) - \ln(\rho(r)) \right\}. \tag{2.2-3}$$

The second term on the right hand side is constant, assuming that θ_i is uniformly distributed, and the last term is independent of θ_i. Thus, the maximization is really over the first term. The first-order necessary condition for optimality is

$$\left. \frac{\partial \ln\left[\rho(\theta_i|r)\right]}{\partial \theta_i} \right|_{\theta_i=\theta_o} = \left. \frac{\partial \ln\left[\rho(r|\theta_i)\right]}{\partial \theta_i} \right|_{\theta_i=\theta_o} = 0. \tag{2.2-4}$$

In order to fulfill this necessary condition, we may work with the right hand expression, rather than the left. Hence, we must compute $\rho(r|\theta_i)$.

Recall that the received signal is given by

$$r(t) = \sqrt{\frac{2E}{T}} \cos(\omega_c t + \theta_i + \theta_m) + w(t) \tag{2.2-5}$$

We may expand this signal using the orthonomal basis

$$\psi_1(t) = \sqrt{\frac{2}{T}} \cos(\omega_c t + \theta_o), \qquad \psi_2(t) = \sqrt{\frac{2}{T}} \sin(\omega_c t + \theta_o). \tag{2.2-6}$$

$$r_1 = \sqrt{\frac{2}{T}} \int_0^T r(\tau) \cos(\omega_c \tau + \theta_o) d\tau, \qquad r_2 = \sqrt{\frac{2}{T}} \int_0^T r(\tau) \sin(\omega_c \tau + \theta_o) d\tau \tag{2.2-7}$$

and obtain (in a mean-square sense)

$$r(t) = r_1 \psi_1(t) + r_2 \psi_2(t). \tag{2.2-8}$$

Performing the integration for r_1 gives

$$r_1 = \sqrt{\frac{2}{T}} \int_0^T \left[\sqrt{\frac{2E}{T}} \cos(\omega_c t + \theta_i + \theta_m) + w(t) \right] \cos(\omega_c t + \theta_o) dt$$

$$= \frac{\sqrt{E}}{T} \int_0^T \left[\cos(\theta_m + \phi) + \cos(2\omega_c t + \theta_i + \theta_o + \theta_m) \right] dt + \sqrt{\frac{2}{T}} \int_0^T w(t) \cos(\omega_c t + \theta_o) dt$$

$$\cong \sqrt{E} \cos(\theta_m + \phi) + \sqrt{\frac{2}{T}} \int_0^T w(t) \cos(\omega_c t + \theta_o) dt = s_1 + n_1$$

for $\omega_c \gg 1$, where $\phi = \theta_i - \theta_o$. A similar process yields for r_2,

$$r_2 = \sqrt{\frac{2}{T}} \int_0^T \left[\sqrt{\frac{2E}{T}} \cos(\omega_c t + \theta_i + \theta_m) + w(t) \right] \sin(\omega_c t + \theta_o) dt$$

$$\cong -\sqrt{E} \sin(\theta_m + \phi) + \sqrt{\frac{2}{T}} \int_0^T w(t) \sin(\omega_c t + \theta_o) dt = s_2 + n_2.$$

Thus, this expansion yields the "in-phase" and "quadrature" components of the received signal. These components are given with respect to the phase θ_o, which is generated as the output of a voltage-controlled oscillator (VCO). The in-phase and quadrature signals are currently obtained in the industry-standard receivers.

Since the noise was assumed to be Gaussian, and since $\mathscr{E}\{r_1\} = s_1$, and $\mathscr{E}\{r_2\} = s_2$, and since the parameters r_1 and r_2 completely describe the received signal under the orthonormal expansion, then we obtain

$$\rho\left(r\middle|\theta_i,\theta_m,\theta_o\right)=\rho\left(r_1\middle|\theta_i,\theta_m,\theta_o\right)\rho\left(r_2\middle|\theta_i,\theta_m,\theta_o\right)=\left(\frac{1}{2\pi\sigma^2}\right)e^{\left(\frac{-(r_1-s_1)^2}{2\sigma^2}\right)}e^{\left(\frac{-(r_2-s_2)^2}{2\sigma^2}\right)}. \quad (2.2\text{-}9)$$

We have defined the variance of $r(t)$ to be given by

$$\sigma^2=\mathscr{E}\left\{n_1^2\right\}=\mathscr{E}\left\{n_2^2\right\}=\mathscr{E}\left\{\left(\sqrt{\tfrac{2}{T}}\int_o^T w(t)\sin(\omega_c t+\theta_o)\right)^2\right\}$$

$$=\tfrac{2}{T}\int_o^T\int_o^T\mathscr{E}\left\{w(t)w(\tau)\right\}\sin(\omega_c\tau+\theta_o)\sin(\omega_c t+\theta_o)d\tau dt$$

$$=\tfrac{2}{T}\int_o^T\int_o^T\left(\tfrac{N_o}{2}\right)\delta(t-\tau)\sin(\omega_c\tau+\theta_o)\sin(\omega_c t+\theta_o)d\tau dt$$

$$=\tfrac{N_o}{T}\int_o^T\sin^2(\omega_c t+\theta_o)dt=\tfrac{N_o}{2T\omega_c}\left(\omega_c T-\tfrac{1}{2}\sin(2\omega_c T+2\theta_o)\right)$$

$$\cong\frac{N_o}{2},\qquad \omega_c\gg 1.$$

Having found the probability density function in the general case, we may now consider each of the modulation shemes in order to evaluate the necessary condition. In each of the cases, we need to consider the probability density function of the modulation angle, θ_m, in order to evaluate this necessary condition.

2.3 The BPSK Likelihood Function Derivation

For the case of binary phase-shift keying, we know that the modulation angle can take on $\theta_m=0,\pi$, and we obtain

$$\rho(\theta_m)=\tfrac{1}{2}\delta(\theta_m)+\tfrac{1}{2}\delta(\theta_m-\pi).$$

Integrating with respect to the modulation gives

$$\rho\left(r\middle|\theta_i,\theta_o\right)=\int_{-\infty}^{\infty}\rho\left(r\middle|\theta_i,\theta_o,\theta_m\right)\rho(\theta_m)d\theta_m$$

$$=\tfrac{1}{2}\rho\left(r\middle|\theta_i,\theta_o,\theta_m=0\right)+\tfrac{1}{2}\rho\left(r\middle|\theta_i,\theta_o,\theta_m=\pi\right)=\left(\frac{1}{4\pi\sigma^2}\right)\left[e^{\left(\frac{-X}{2\sigma^2}\right)}+e^{\left(\frac{-Y}{2\sigma^2}\right)}\right] \quad (2.3\text{-}1)$$

where

$$X = (r_1 - s_1)^2 + (r_2 - s_2)^2\Big|_{\theta_m=0} = r_1^2 + r_2^2 + s_1^2 + s_2^2 - 2r_1s_1 - 2r_2s_2\Big|_{\theta_m=0}$$

$$= r_1^2 + r_2^2 + E - 2\sqrt{E}\left(r_1\cos\phi - r_2\sin\phi\right) = a - 2\sqrt{E}\,z$$

where $a = r_1^2 + r_2^2 + E$, and $z = r_1\cos\phi - r_2\sin\phi$. Similarly,

$$Y = (r_1 - s_1)^2 + (r_2 - s_2)^2\Big|_{\theta_m=\pi} = r_1^2 + r_2^2 + s_1^2 + s_2^2 - 2r_1s_1 - 2r_2s_2\Big|_{\theta_m=\pi}$$

$$= r_1^2 + r_2^2 + E + 2\sqrt{E}\left(r_1\cos\phi - r_2\sin\phi\right) = a + 2\sqrt{E}\,z.$$

Substituting X and Y into (2.3-1) yields

$$\rho\left(r\middle|\theta_i,\theta_o\right) = \left(\frac{1}{4\pi\sigma^2}\right)\left[e^{\left(\frac{-(a-2\sqrt{E}z)}{2\sigma^2}\right)} + e^{\left(\frac{-(a+2\sqrt{E}z)}{2\sigma^2}\right)}\right] = \left(\frac{1}{4\pi\sigma^2}\right)e^{\left(\frac{-a}{2\sigma^2}\right)}\left[e^{\left(\frac{\sqrt{E}z}{\sigma^2}\right)} + e^{\left(\frac{-\sqrt{E}z}{\sigma^2}\right)}\right]$$

$$= \left(\frac{1}{2\pi\sigma^2}\right)e^{\left(\frac{-a}{2\sigma^2}\right)}\cosh\left(\frac{\sqrt{E}z}{\sigma^2}\right). \qquad (2.3\text{-}2)$$

Defining now

$$W = \frac{\sqrt{E}z}{\sigma^2} = \frac{\sqrt{E}}{\sigma^2}\left(r_1\cos\phi - r_2\sin\phi\right)$$

$$= \frac{\sqrt{E}}{\sigma^2}\int_0^T\left(\sqrt{\frac{2}{T}}\right)\left(r(t)\cos(\omega_c t + \theta_o)\cos\phi - r(t)\sin(\omega_c t + \theta_o)\sin\phi\right)dt$$

$$= \sqrt{\frac{2E}{T\sigma^4}}\int_0^T r(t)\cos(\omega_c t + \theta_o + \phi)\,dt$$

$$= \frac{2E}{N_o}\int_0^T gr(t)\cos(\omega_c t + \theta_i)dt \qquad (2.3\text{-}3)$$

where $g = \sqrt{\frac{2}{TE}}$. We have introduced the constant g, since its presence in the form of an AGC circuit allows the resulting scale factors to be applicable to physical variables in industry-standard receivers. Substituting (2.3-3) into (2.3-2) gives

$$\rho\left(r\middle|\theta_i,\theta_o\right)=\left(\frac{1}{2\pi\sigma^2}\right)e^{\frac{-(r_1^2+r_2^2+E)}{2\sigma^2}}\cosh\left[\frac{2E}{N_o}\int_0^T gr(t)\cos(\omega_c t+\theta_i)dt\right]=\rho\left(r\middle|\theta_i\right). \quad (2.3\text{-}4)$$

Not surprisingly, we see that $\rho\left(r\middle|\theta_i,\theta_o\right)$ is independent of θ_o. Thus, the first-order necessary condition becomes

$$\frac{\partial}{\partial\theta_i}\ln\left(r\middle|\theta_i\right)\Bigg|_{\theta_i=\theta_o}=$$

$$=\frac{\partial}{\partial\theta_i}\left[\ln\left(\left(\frac{1}{2\pi\sigma^2}\right)e^{\frac{-(r_1^2+r_2^2+E)}{2\sigma^2}}\right)+\ln\cosh\left(\frac{2E}{N_o}\int_0^T gr(t)\cos(\omega_c t+\theta_i)dt\right)\right]_{\theta_i=\theta_o}$$

$$=\left[\tanh\left(\frac{2E}{N_o}\int_0^T gr(t)\cos(\omega_c t+\theta_i)dt\right)\right]\left[-\frac{2E}{N_o}\int_0^T gr(t)\sin(\omega_c t+\theta_i)dt\right]_{\theta_i=\theta_o}$$

$$=\frac{2E}{N_o}\tanh\left(\frac{2E}{N_o}I\right)Q=0$$

or $\frac{2E}{N_o}\hat{I}Q=0$, where

$$I=g\int_0^T r(t)\cos(\omega_c t+\theta_o)dt \quad (2.3\text{-}5a)$$

$$Q=-g\int_0^T r(t)\sin(\omega_c t+\theta_o)dt=g\int_0^T r(t)\cos(\omega_c t+\theta_o+90^\circ)dt \quad (2.3\text{-}5b)$$

and $\hat{I}=\tanh\left(\frac{2E}{N_o}I\right)$. A block diagram of this estimator may be obtained from this proceedure, and is shown in Figure 2.3-1

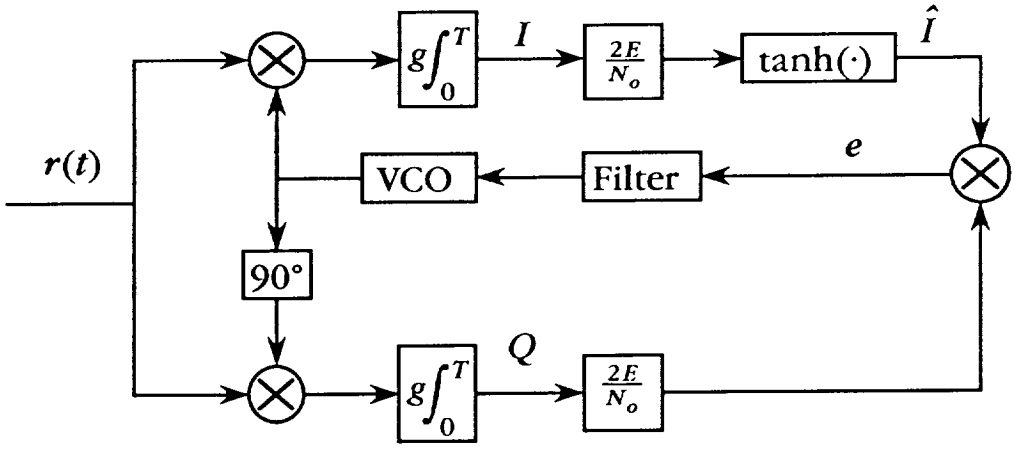

Figure 2.3-1 BPSK Carrier Phase Tracking Loop

2.4 The QPSK Likelihood Function

If the modulation is chosen to be quadrature phase-shift keying (QPSK) then we know that $\theta_m = \frac{\pi}{4}, \frac{3\pi}{4}, \frac{-\pi}{4}$ or $\frac{-3\pi}{4}$ and

$$\rho(\theta_m) = \tfrac{1}{4}\left[\delta(\theta_m - \pi/4) + \delta(\theta_m - 3\pi/4) + \delta(\theta_m + \pi/4) + \delta(\theta_m + 3\pi/4)\right]. \tag{2.4-1}$$

We now integrate with respect to the modulation probability and obtain

$$\rho\left(r|\theta_i,\theta_o\right) = \int_{-\infty}^{\infty} \rho\left(r|\theta_i,\theta_o,\theta_m\right)\rho(\theta_m)d\theta_m$$

$$= \tfrac{1}{4}\left[\rho\left(r|\theta_i,\theta_o,\theta_m = \tfrac{\pi}{4}\right) + \rho\left(r|\theta_i,\theta_o,\theta_m = \tfrac{3\pi}{4}\right) + \rho\left(r|\theta_i,\theta_o,\theta_m = \tfrac{-\pi}{4}\right) + \rho\left(r|\theta_i,\theta_o,\theta_m = \tfrac{-3\pi}{4}\right)\right]$$

$$= \left(\tfrac{1}{4}\right)\left(\frac{1}{2\pi\sigma^2}\right)\sum_{i=1}^{4} e^{\frac{-X_i}{2\sigma^2}} \tag{2.4-2}$$

where

$$X_1 = (r_1 - s_1)^2 + (r_2 - s_2)^2\Big|_{\theta_m=\frac{\pi}{4}} = r_1^2 + r_2^2 + s_1^2 + s_2^2 - 2r_1s_1 - 2r_2s_2\Big|_{\theta_m=\frac{\pi}{4}}$$

$$= r_1^2 + r_2^2 + E - r_1\sqrt{2E}\left(\cos\phi - \sin\phi\right) + r_2\sqrt{2E}\left(\cos\phi + \sin\phi\right) \tag{2.4-3}$$

$$X_2 = (r_1 - s_1)^2 + (r_2 - s_2)^2\Big|_{\theta_m=\frac{3\pi}{4}} = r_1^2 + r_2^2 + s_1^2 + s_2^2 - 2r_1s_1 - 2r_2s_2\Big|_{\theta_m=\frac{3\pi}{4}}$$

$$= r_1^2 + r_2^2 + E + r_1\sqrt{2E}\left(\cos\phi + \sin\phi\right) + r_2\sqrt{2E}\left(\cos\phi - \sin\phi\right) \tag{2.4-4}$$

$$X_3 = (r_1 - s_1)^2 + (r_2 - s_2)^2\Big|_{\theta_m = \frac{-3\pi}{4}} = r_1^2 + r_2^2 + s_1^2 + s_2^2 - 2r_1 s_1 - 2r_2 s_2\Big|_{\theta_m = \frac{-3\pi}{4}}$$

$$= r_1^2 + r_2^2 + E + r_1\sqrt{2E}\left(\cos\phi - \sin\phi\right) - r_2\sqrt{2E}\left(\cos\phi + \sin\phi\right) \tag{2.4-5}$$

$$X_4 = (r_1 - s_1)^2 + (r_2 - s_2)^2\Big|_{\theta_m = \frac{-\pi}{4}} = r_1^2 + r_2^2 + s_1^2 + s_2^2 - 2r_1 s_1 - 2r_2 s_2\Big|_{\theta_m = \frac{-\pi}{4}}$$

$$= r_1^2 + r_2^2 + E - r_1\sqrt{2E}\left(\cos\phi + \sin\phi\right) - r_2\sqrt{2E}\left(\cos\phi - \sin\phi\right) \tag{2.4-6}$$

Substituting (2.4-3)-(2.4-6) into (2.4-2) gives

$$\rho\left(r\middle|\theta_i, \theta_o\right) = \left(\tfrac{1}{4}\right)\left(\tfrac{1}{2\pi\sigma^2}\right)\left(e^{\frac{-a}{2\sigma^2}}\right)\left(e^{\alpha z_1} + e^{\alpha z_2} + e^{\alpha z_3} + e^{\alpha z_4}\right) \tag{2.4-7}$$

where we define

$a = r_1^2 + r_2^2 + E$, $\alpha = -\sqrt{\frac{E}{2\sigma^4}}$ and

$$z_1 = -r_1\left(\cos\phi - \sin\phi\right) + r_2\left(\cos\phi + \sin\phi\right) \tag{2.4-8a}$$

$$z_2 = r_1\left(\cos\phi + \sin\phi\right) + r_2\left(\cos\phi - \sin\phi\right) \tag{2.4-8b}$$

$$z_3 = r_1\left(\cos\phi - \sin\phi\right) - r_2\left(\cos\phi + \sin\phi\right) = -z_1 \tag{2.4-8c}$$

$$z_4 = -r_1\left(\cos\phi + \sin\phi\right) - r_2\left(\cos\phi - \sin\phi\right) = -z_2 \tag{2.4-8d}$$

$$W = \left(e^{\alpha z_1} + e^{\alpha z_2} + e^{\alpha z_3} + e^{\alpha z_4}\right) \tag{2.4-9}$$

Under these definitions, we obtain

$$W = 2\cosh(\alpha z_1) + 2\cosh(\alpha z_2) = W_1 + W_2.$$

Simplifying, we obtain

$$W_1 = 2\cosh\left[\alpha\left(-r_1(\cos\phi - \sin\phi) + r_2(\sin\phi + \cos\phi)\right)\right]$$

$$= 2\cosh\left[\sqrt{\frac{E}{2\sigma^4}}\sqrt{\frac{2}{T}}\int_0^T r(t)\left\{\cos(\omega_c t + \theta_o)[\cos\phi - \sin\phi] - \sin(\omega_c t + \theta_o)[\cos\phi + \sin\phi]\right\}dt\right]$$

$$= 2\cosh\left[\frac{E}{\sqrt{2\sigma^2}}\int_0^T gr(t)\{\cos(\omega_c t + \theta_i) - \sin(\omega_c t + \theta_i)\}dt\right] \tag{2.4-10}$$

$$W_2 = 2\cosh\left[\alpha\left(r_1(\cos\phi + \sin\phi) + r_2(\cos\phi - \sin\phi)\right)\right]$$

$$= 2\cosh\left[-\sqrt{\frac{E}{2\sigma^4}}\sqrt{\frac{2}{T}}\int_0^T r(t)\{\cos(\omega_c t + \theta_o)[\cos\phi + \sin\phi] + \sin(\omega_c t + \theta_o)[\cos\phi - \sin\phi]\}dt\right]$$

$$= 2\cosh\left[\frac{E}{\sqrt{2\sigma^2}}\int_0^T gr(t)\{\cos(\omega_c t + \theta_i) + \sin(\omega_c t + \theta_i)\}dt\right]. \tag{2.4-11}$$

Thus (2.4-7) can be written as:

$$\rho\left(r\middle|\theta_i,\theta_o\right) = \left(\tfrac{1}{4}\right)\left(\frac{1}{2\pi\sigma^2}\right)\left(e^{\frac{-a}{2\sigma^2}}\right)\left(2\cosh(U) + 2\cosh(V)\right) \tag{2.4-12}$$

where

$$U = \left[\frac{E}{\sqrt{2\sigma^2}}\int_0^T gr(t)\{\cos(\omega_c t + \theta_i) - \sin(\omega_c t + \theta_i)\}dt\right] \tag{2.4-13a}$$

$$V = \left[\frac{E}{\sqrt{2\sigma^2}}\int_0^T gr(t)\{\cos(\omega_c t + \theta_i) + \sin(\omega_c t + \theta_i)\}dt\right] \tag{2.4-13b}$$

We now consider the change of variables

$$\begin{bmatrix} U \\ V \end{bmatrix} = \begin{bmatrix} X - Y \\ X + Y \end{bmatrix} = \begin{bmatrix} 1 & -1 \\ 1 & 1 \end{bmatrix}\begin{bmatrix} X \\ Y \end{bmatrix} \tag{2.4-14}$$

Solving for X and Y in terms of U and V, we have

$$\begin{bmatrix} X \\ Y \end{bmatrix} = \begin{bmatrix} 1 & -1 \\ 1 & 1 \end{bmatrix}^{-1}\begin{bmatrix} U \\ V \end{bmatrix} = \left(\tfrac{1}{2}\right)\begin{bmatrix} 1 & 1 \\ -1 & 1 \end{bmatrix}\begin{bmatrix} U \\ V \end{bmatrix} = \left(\tfrac{1}{2}\right)\begin{bmatrix} U + V \\ -U + V \end{bmatrix}$$

$$= \begin{bmatrix} \frac{E}{\sqrt{2}\sigma^2}\int_0^T gr(t)\cos(\omega_c t + \theta_i)dt \\ \frac{E}{\sqrt{2}\sigma^2}\int_0^T gr(t)\sin(\omega_c t + \theta_i)dt \end{bmatrix}. \tag{2.4-15}$$

We use the following property of the hyperbolic cosine

$$\cosh(x-y)+\cosh(x+y) = 2\cosh(x)\cosh(y) \tag{2.4-16}$$

to see that

$$\cosh(U)+\cosh(V) = \cosh(X-Y)+\cosh(X+Y) = 2\cosh(X)\cosh(Y).$$

We now rewrite (2.4-12) as

$$\rho\left(r\middle|\theta_i,\theta_o\right) = \left(\frac{1}{2\pi\sigma^2}\right)\left(e^{\frac{-(r_1^2+r_2^2+E)}{2\sigma^2}}\right)\left(\cosh(X)\cosh(Y)\right). \tag{2.4-17}$$

Evaluating the first-order necessary condition gives

$$\frac{\partial}{\partial\theta_i}\ln\left[\rho\left(r\middle|\theta_i\right)\right]\Big|_{\theta_i=\theta_o} = \frac{\partial}{\partial\theta_i}\left[\ln\left(\left(\frac{1}{2\pi\sigma^2}\right)e^{\frac{-(r_1^2+r_2^2+E)}{2\sigma^2}}\right)+\ln\cosh(X)+\ln\cosh(Y)\right]_{\theta_i=\theta_o}$$

$$= \tanh\left[\frac{E}{\sqrt{2}\sigma^2}\int_0^T gr(t)\cos(\omega_c t+\theta_i)dt\right]\left[-\frac{E}{\sqrt{2}\sigma^2}\int_0^T gr(t)\sin(\omega_c t+\theta_i)dt\right]_{\theta_i=\theta_o} +$$

$$+\tanh\left[\frac{E}{\sqrt{2}\sigma^2}\int_0^T gr(t)\sin(\omega_c t+\theta_i)dt\right]\left[\frac{E}{\sqrt{2}\sigma^2}\int_0^T gr(t)\cos(\omega_c t+\theta_i)dt\right]_{\theta_i=\theta_o}$$

$$= \frac{E}{\sqrt{2}\sigma^2}\tanh\left(\frac{E}{\sqrt{2}\sigma^2}I\right)Q - \frac{E}{\sqrt{2}\sigma^2}\tanh\left(\frac{E}{\sqrt{2}\sigma^2}Q\right)I = 0.$$

Thus, the necessary condition gives rise to the error signal

$$\varepsilon(t) = \frac{\sqrt{2}E}{N_o}\left[\tanh\left(\frac{\sqrt{2}E}{N_o}I\right)Q - \tanh\left(\frac{\sqrt{2}E}{N_o}Q\right)I\right] \tag{2.4-18}$$

where we may define

$$\hat{Q} = \tanh\left(\frac{\sqrt{2E}}{N_o} Q\right), \quad \hat{I} = \tanh\left(\frac{\sqrt{2E}}{N_o} I\right). \tag{2.4-19}$$

A block diagram for the implementation of the necessary condition is given in Figure 2.4-1.

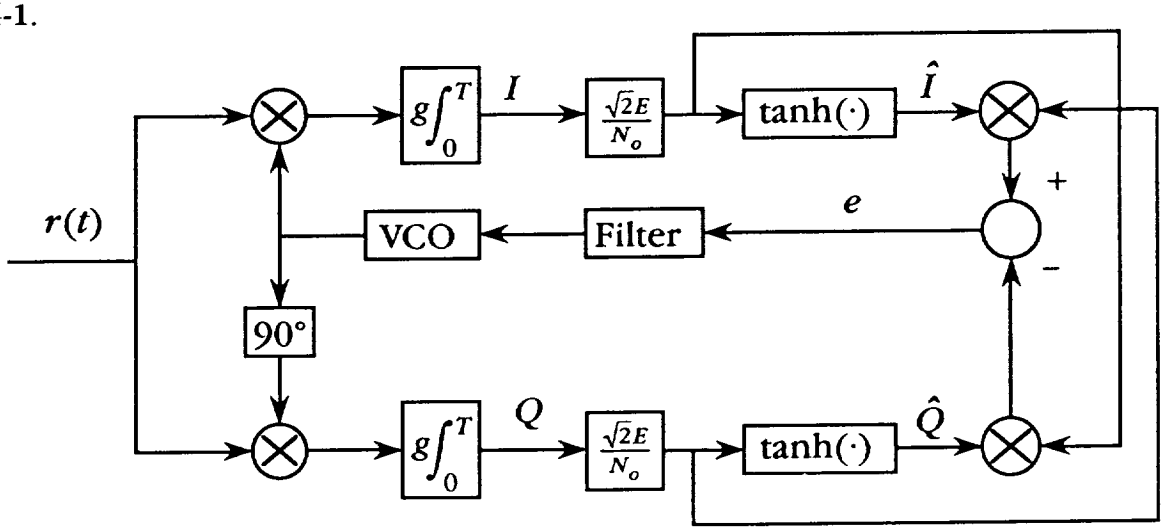

Figure 2.4-1. A Block Diagram Realization of the QPSK MAP estimator

2.5 Higher-Order PSK

We now consider the (higher order) M-ary phase-shift keying, where

$$M = 2^n \qquad 2 < n - \text{integer} \tag{2.5-1}$$

and the modulation angle can take on the values

$$\theta_m = \pm\frac{(2k+1)\pi}{2^n}, \quad k = 0, \cdots, 2^{n-1} - 1, \tag{2.5-2}$$

giving the probability density function

$$\rho(\theta_m) = \frac{1}{2^n} \sum_{k=0}^{2^{n-1}-1} \delta\left(\theta_m - \frac{(2k+1)\pi}{2^n}\right) + \delta\left(\theta_m + \frac{(2k+1)\pi}{2^n}\right). \tag{2.5-3}$$

Integrating with respect to the probability density function gives

$$\rho\left(r\middle|\theta_i, \theta_o\right) = \int_{-\infty}^{\infty} \rho\left(r\middle|\theta_i, \theta_o, \theta_m\right) \rho(\theta_m) d\theta_m$$

$$= \frac{1}{2^n} \sum_{k=0}^{2^{n-1}-1} \rho\left(r \middle| \theta_i, \theta_o, \theta_m = \frac{(2k+1)\pi}{2^n} \right) + \rho\left(r \middle| \theta_i, \theta_o, \theta_m = -\frac{(2k+1)\pi}{2^n} \right)$$

$$= \left(\frac{1}{2^n} \right) \left(\frac{1}{2\pi\sigma^2} \right) \sum_{k=1}^{2^{n-1}} e^{\left(\frac{-X_k}{2\sigma^2} \right)} + e^{\left(\frac{-X_{-k}}{2\sigma^2} \right)} \qquad (2.5\text{-}4)$$

where for $k = 1, \cdots, 2^{n-1}$,

$$X_k = (r_1 - s_1)^2 + (r_2 - s_2)^2 \Big|_{\theta_m = \frac{(2k+1)\pi}{2^n}} = r_1^2 + r_2^2 + s_1^2 + s_2^2 - 2r_1 s_1 - 2r_2 s_2 \Big|_{\theta_m = \frac{(2k+1)\pi}{2^n}}$$

$$= r_1^2 + r_2^2 + E - 2r_1\sqrt{E}\cos\left(\frac{(2k+1)\pi}{M} + \phi \right) + 2r_2\sqrt{E}\sin\left(\frac{(2k+1)\pi}{M} + \phi \right)$$

$$= r_1^2 + r_2^2 + E - 2r_1\sqrt{E}\left[\cos\left(\frac{(2k+1)\pi}{M} \right)\cos(\phi) - \sin\left(\frac{(2k+1)\pi}{M} \right)\sin(\phi) \right]$$

$$+2r_2\sqrt{E}\left[\sin\left(\frac{(2k+1)\pi}{M} \right)\cos(\phi) + \cos\left(\frac{(2k+1)\pi}{M} \right)\sin(\phi) \right]$$

$$= a - 2\sqrt{E}\left(r_1\left[C_k\cos(\phi) - S_k\sin(\phi) \right] - r_2\left[S_k\cos(\phi) + C_k\sin(\phi) \right] \right), \qquad (2.5\text{-}5)$$

and where

$$\ell = 2^{n-1}, \quad a = r_1^2 + r_2^2 + E, \quad C_k = \cos\left(\frac{(2k+1)\pi}{M} \right), \quad S_k = \sin\left(\frac{(2k+1)\pi}{M} \right). \qquad (2.5\text{-}6)$$

We also have for $k = 1, \cdots, \ell$,

$$X_{-k} = (r_1 - s_1)^2 + (r_2 - s_2)^2 \Big|_{\theta_m = -\frac{(2k+1)\pi}{2^n}} = r_1^2 + r_2^2 + s_1^2 + s_2^2 - 2r_1 s_1 - 2r_2 s_2 \Big|_{\theta_m = -\frac{(2k+1)\pi}{2^n}}$$

$$= a - 2\sqrt{E}\left(r_1\left[C_k\cos(\phi) + S_k\sin(\phi) \right] + r_2\left[S_k\cos(\phi) - C_k\sin(\phi) \right] \right). \qquad (2.5\text{-}7)$$

We now define, for $k = 1, \cdots, \ell$,

$$z_k = -r_1\left[C_k\cos(\phi) - S_k\sin(\phi) \right] + r_2\left[S_k\cos(\phi) + C_k\sin(\phi) \right] \qquad (2.5\text{-}8a)$$

$$z_{-k} = -r_1\left[C_k\cos(\phi) + S_k\sin(\phi) \right] - r_2\left[S_k\cos(\phi) - C_k\sin(\phi) \right] \qquad (2.5\text{-}8b)$$

and note that for $k = 1, \cdots, \ell$,

$$X_k = a - 2\sqrt{E}\ z_k, \qquad X_{-k} = a - 2\sqrt{E}\ z_{-k} \tag{2.5-9}$$

Since $C_{\ell-k+1} = -C_k$ and $S_{\ell-k+1} = -S_k$, then

$$z_k = -z_{-(\ell-k+1)}. \tag{2.5-10}$$

Define now,

$$W = \sum_{k=1}^{\ell} e^{\beta z_k} + e^{\beta z_{-k}}$$

and note that

$$W = \sum_{k=1}^{\ell} e^{\beta z_k} + e^{\beta z_{-(\ell-k+1)}} = \sum_{k=1}^{\ell/2} e^{\beta z_k} + e^{\beta z_{-(\ell-k+1)}} + e^{\beta z_{-k}} + e^{\beta z_{\ell-k+1}}$$

$$= \sum_{k=1}^{\ell/2} 2\cosh(\beta z_k) + 2\cosh(\beta z_{-k}). \tag{2.5-11}$$

Examining the term

$$\beta z_k = -\beta r_1\left[C_k \cos(\phi) - S_k \sin(\phi)\right] + \beta r_2\left[S_k \cos(\phi) + C_k \sin(\phi)\right]$$

$$= -\frac{\beta g}{g}\left(\sqrt{\frac{2}{T}}\int_0^T r(\tau)\cos(\omega_c\tau + \theta_o)d\tau\right)\left[C_k \cos(\phi) - S_k \sin(\phi)\right]$$

$$+\frac{\beta g}{g}\left(\sqrt{\frac{2}{T}}\int_0^T r(\tau)\sin(\omega_c\tau + \theta_o)d\tau\right)\left[S_k \cos(\phi) + C_k \sin(\phi)\right]$$

$$= \frac{gE}{\sigma^2}\int_0^T r(\tau)\Big\{-\cos(\omega_c\tau + \theta_o)\left[C_k \cos(\phi) - S_k \sin(\phi)\right] +$$

$$+\sin(\omega_c\tau + \theta_o)\left[S_k \cos(\phi) + C_k \sin(\phi)\right]\Big\}d\tau$$

$$= \frac{gE}{\sigma^2}\int_0^T r(\tau)\Big\{-C_k \cos(\omega_c\tau + \theta_i) + S_k \sin(\omega_c\tau + \theta_i)\Big\}d\tau$$

$$= -\left(\frac{C_k E}{\sigma^2}\right)I' - \left(\frac{S_k E}{\sigma^2}\right)Q' = -\gamma_k I' - \mu_k Q' \tag{2.5-12}$$

for

$$\gamma_k = \frac{C_k E}{\sigma^2} = \frac{2C_k E}{N_o}, \qquad \mu_k = \frac{S_k E}{\sigma^2} = \frac{2S_k E}{N_o} \tag{2.5-13a}$$

$$I' = g\int_o^T r(t)\cos(\omega_c t + \theta_i)dt, \qquad Q' = -g\int_o^T r(t)\sin(\omega_c t + \theta_i)dt. \tag{2.5-13b}$$

Similarly,

$$\beta z_{-k} = -\beta r_1\left[C_k\cos(\phi) + S_k\sin(\phi)\right] - \beta r_2\left[S_k\cos(\phi) - C_k\sin(\phi)\right]$$

$$= -\left(\frac{C_k E}{\sigma^2}\right)I' + \left(\frac{S_k E}{\sigma^2}\right)Q' = -\gamma_k I' + \mu_k Q'. \tag{2.5-14}$$

Thus, W becomes

$$W = \sum_{k=1}^{n/2} 2\cosh(\gamma_k I' + \mu_k Q') + 2\cosh(-\gamma_k I' + \mu_k Q') = \sum_{k=1}^{n/2} 4\cosh(\gamma_k I')\cosh(\mu_k Q'). \tag{2.5-15}$$

In this case, we may write the probability density function as

$$\rho\left(r\middle|\theta_i,\theta_o\right) = \left(\frac{1}{2^n}\right)\left(\frac{1}{2\pi\sigma^2}\right)\sum_{k=1}^{2^{n-1}} e^{\left(\frac{-X_k}{2\sigma^2}\right)} + e^{\left(\frac{-X_{-k}}{2\sigma^2}\right)} = \left(\frac{1}{2^n}\right)\left(\frac{1}{2\pi\sigma^2}\right)\left(e^{-\frac{a}{2\sigma^2}}\right)W \tag{2.5-16a}$$

and

$$\ln\left[\rho\left(r\middle|\theta_i,\theta_o\right)\right] = \ln\left(\left(\frac{1}{2^{n+1}\pi\sigma^2}\right)e^{-\frac{a}{2\sigma^2}}\right) + \ln(W). \tag{2.5-16b}$$

Evaluating the first-order necessary condition, gives

$$\left.\frac{\partial \ln\left[\rho\left(R\middle|\theta_i\right)\right]}{\partial\theta_i}\right|_{\theta_i=\theta_o} = \left.\frac{\partial W/\partial\theta_i}{W}\right|_{\theta_i=\theta_o}$$

and

$$\left.\frac{\partial W}{\partial\theta_i}\right|_{\theta_i=\theta_o} = 4\sum_{k=1}^{n/2}\gamma_k\sinh(\gamma_k I')\cosh(\mu_k Q')\left(\frac{\partial I'}{\partial\theta_i}\right) + \mu_k\cosh(\gamma_k I')\sinh(\mu_k Q')\left(\frac{\partial Q'}{\partial\theta_i}\right)\Bigg|_{\theta_i=\theta_o}.$$

In order to evaluate this expression, we note that

$$\left(\frac{\partial I'}{\partial \theta_i}\right)\Bigg|_{\theta_i=\theta_o} = Q'\big|_{\theta_i=\theta_o} = Q, \quad \left(\frac{\partial Q'}{\partial \theta_i}\right)\Bigg|_{\theta_i=\theta_o} = -I'\big|_{\theta_i=\theta_o} = -I \tag{2.5-17}$$

and so

$$\left.\frac{\partial W}{\partial \theta_i}\right|_{\theta_i=\theta_o} = 4\sum_{k=1}^{1/2} \gamma_k Q \sinh(\gamma_k I)\cosh(\mu_k Q) - \mu_k I \cosh(\gamma_k I)\sinh(\mu_k Q)$$

$$= 4\sum_{k=1}^{1/2} \gamma_k Q \tanh(\gamma_k I)\cosh(\gamma_k I)\cosh(\mu_k Q) - \mu_k I \cosh(\gamma_k I)\cosh(\mu_k Q)\tanh(\mu_k Q)$$

$$= 4\sum_{k=1}^{1/2} \cosh(\gamma_k I)\cosh(\mu_k Q)\left(\gamma_k Q \tanh(\gamma_k I) - \mu_k I \tanh(\mu_k Q)\right). \tag{2.5-18}$$

Thus the necessary condition of optimaltiy gives rise to the error function

$$\varepsilon(t) = \frac{\sum_{k=1}^{1/2} \cosh(\gamma_k I)\cosh(\mu_k Q)\left(\gamma_k Q \tanh(\gamma_k I) - \mu_k I \tanh(\mu_k Q)\right)}{\sum_{k=1}^{1/2} \cosh(\gamma_k I)\cosh(\mu_k Q)}$$

or

$$\varepsilon(t) = \sum_{k=1}^{1/2} \frac{\gamma_k Q \tanh(\gamma_k I) - \mu_k I \tanh(\mu_k Q)}{1 + \sum_{\substack{j=1 \\ j\neq k}}^{1/2} \frac{\cosh(\gamma_j I)\cosh(\mu_j Q)}{\cosh(\gamma_k I)\cosh(\mu_k Q)}}. \tag{2.5-19}$$

2.6 A Comparison of the Various Strategies

In comparing the various strategies, we observe the error function. In each case, it is a function of the in-phase and quadrature components of the signal. For higher order strategies, this becomes increasingly complex. We have primarily considered only strategies that are powers of 2, although others could be considered. This restriction corresponds to the sending of n bits of data in each symbol. This also gives rise to a great deal of symmetry in the derivation.

In Figures 2.6-1 through 2.6-4, we see the error signals for BPSK, QPSK, 8PSK and 16PSK. assuming a 5 dB signal-to-noise ratio. In each case we see rounded edges associated with a "soft-decision" structure. Indeed, as the order increases, the edges seem to become more rounded, indicating the difficulty of making a decision.

Another feature of the increasing order is that the magnitude of the error function decreases. Even though I and Q are plotted on the same scale, we see that the error has decreased by an entire order of magnitude from BPSK to 16PSK. This is also indicative of the conservatism required in executing the higher-order estimation.

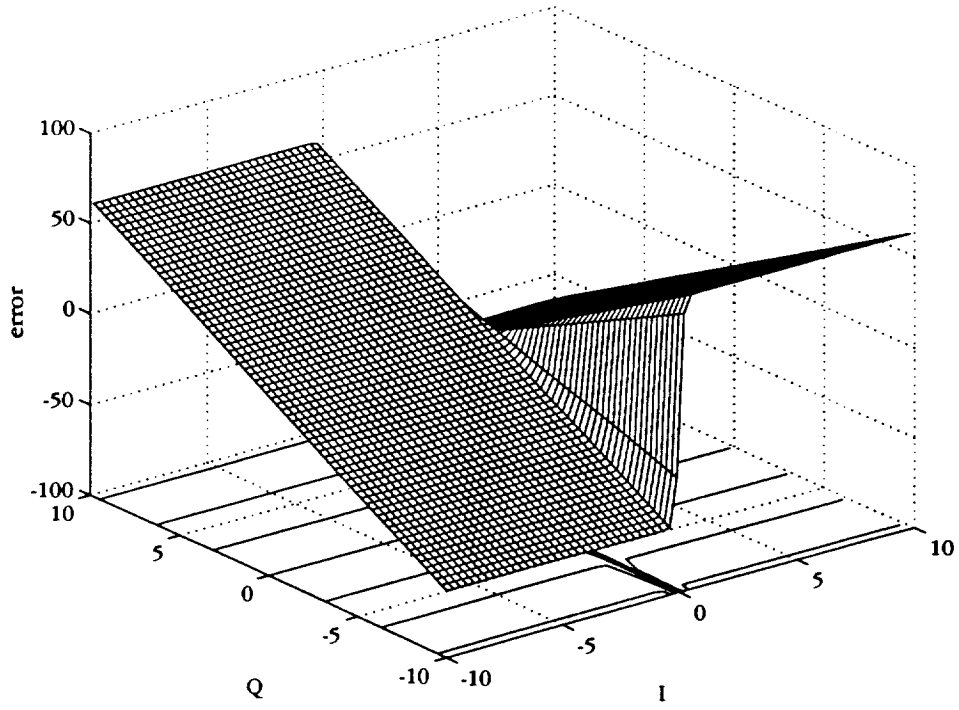

Figure 2.6-1. BPSK Error Function

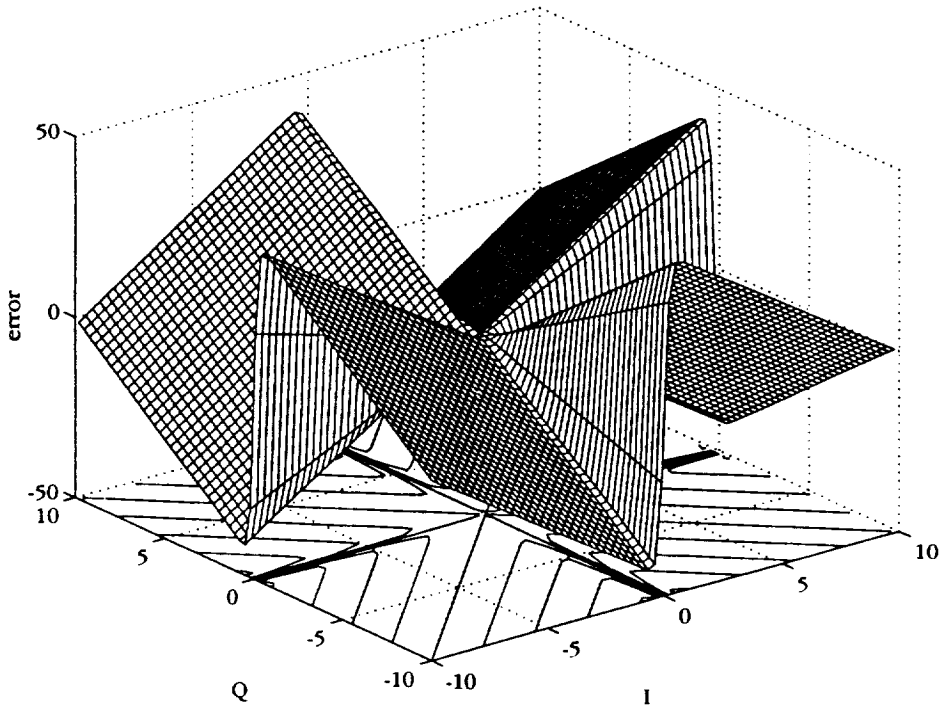

Figure 2.6-2 QPSK Error Function

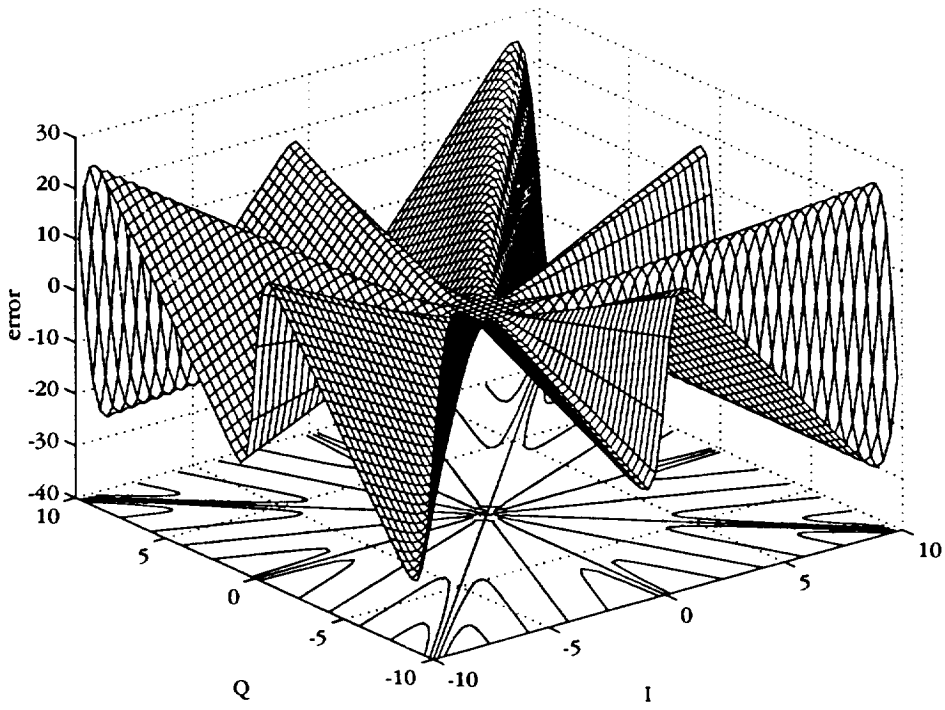

Figure 2.6-3 8PSK Error Function

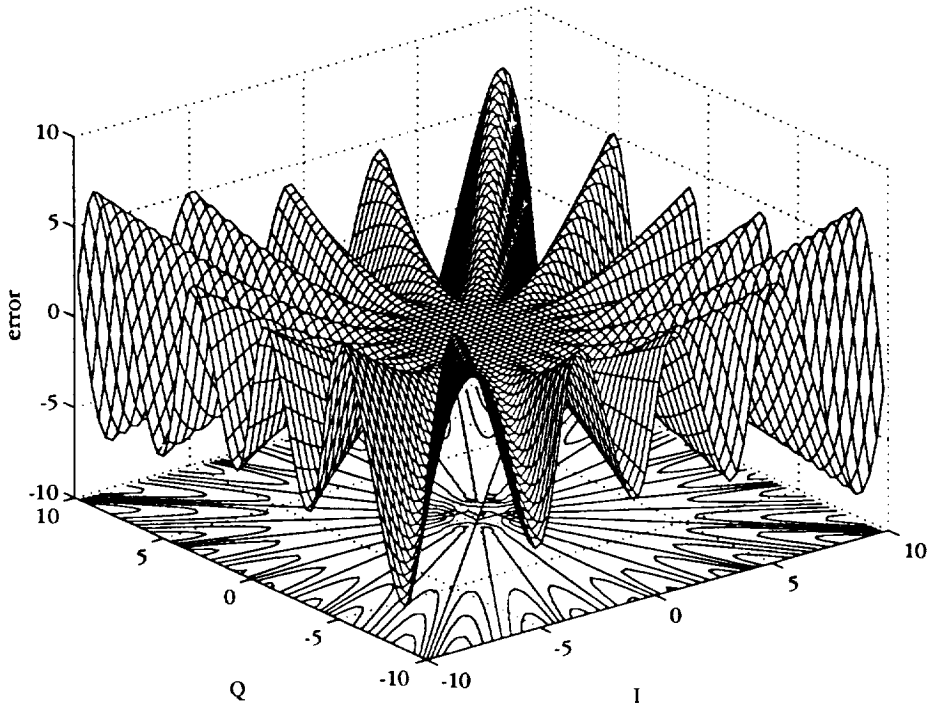

Figure 2.6-4. 16PSK Error Function

SECTION 3. MPSK CARRIER TRACKING HARDWARE PROJECT

3.1 INTRODUCTION

To facilitate the testing of carrier synchronization techniques for MPSK systems a testbed is being constructed. The testbed is made up of two parts. The first of these is the carrier synchronizer. The second is the demodulator.

The carrier synchronizer is capable of tracking BPSK, QPSK, 8PSK, and 16PSK signals. The IF frequency is 15 MHz and the data rate can be 500k symbol-per second (sps), 1Msps, 2Msps, or 4 Msps. The current synchronizer configuration uses the high SNR approximation to MAP estimation of carrier phase to track the received signal. It is a digital design. Its inputs are digital samples of the I and Q channels which it gets from the demodulator. This is shown in Figure 3.1-1. The synchronizer generates a signal which is transferred to a Stanford Telecom's 1272 NCO board. This circuit generates the sine and cosine signals which are used to drive the demodulator.

In Figure 3.1-2 the demodulator is shown. The input signal for testing carrier tracking is simply a 15 MHz carrier. Since an M-ARY PSK signal has M ambiguous lock points in its constellation transmitting the same symbol repeatedly is equivalent to randomly switching between all of the M symbols, in so far as carrier tracking is concerns. This makes it possible to create a simplified test environment utilizing nothing more than a 15 MHz carrier as an input. The demodulator utilizes the quadrature structure and both the I and Q branches are sampled to provide the digital information required for the carrier synchronizer. Both the demodulator and the carrier synchronizer require a symbol clock and this must be provided by a function generator. The system has been designed to allow for easy conversion to an actual MPSK receiver environment.

3.2 THE CARRIER SYNCHRONIZER

There are four digital circuit cards arranged along a backplane that make up the main part of the carrier synchronizer. These are shown in Figure 3.2-1. Referring also to Figures 3.1-1 and 3.1-2 there are several different functions provided in this unit. Starting at the 8 bit I and Q inputs, two 512k EPROMs are used to generate the sine of the phase error during a symbol period. The 16 bit sine of the phase error is used as the tracking error signal and is passed to the loop filter. The loop filter's transfer function is 1 + a/s and is implemented with the use of two 16 bit ALU's; one for the accumulator and one for

the sumer. DC loop gain and the filter cut-off frequency are adjusted by the use of barrel-shifters in the loop filter circuit which can divide a digital word by powers of two. The input to the NCO is a 32 bit word representing the frequency it is to output during the next symbol period. The 32 bit word must contain the quiescent frequency and any error signal component that the loop generates. The quiescent frequency is generated by the sweep circuitry and added to the error signal using two cascaded 16 ALU's. The sweep circuitry can output a static 32 word for a quiescent 15 MHz or it can be swept to better match the test input signal. The sweep speed and step size can be changed from the front panel. Sweep controls are manual in the carrier synchronizer's current design.

Figure 3.1-1 shows a phase shifter incorporated with the sweep circuitry. This was done to facilitate ambiguity resolution. The phase shifter can introduce a phase shift to realign the NCO frequency with a different MPSK phase vector. Since ambiguity resolution is not required for carrier synchronization the current synchronizer configuration does not include the phase shifter circuitry. However, its design has been completed for future use.

The 32 bit word that is sent to the Stanford Telecom NCO board is transmitted in byte-serial fashion over an 8 bit bus. The four bytes are clocked into the NCO during a symbol period by the use of special timing circuits. These circuits use tapped delay chips and XOR gates to generate four clock pulses from a single symbol clock pulse.

One other circuit that is incorporated in the synchronizer design is the lock detector circuit. In a future version of the synchronizer, lock detection will be automatic and tied into the sweep circuitry to initiate and terminate carrier sweeping. In a full-up receiver design this will assist in achieving symbol synchronization and ultimately in achieving carrier synchronization.

The carrier synchronizer is a 10 inch high 19 inch wide rack mountable unit. The front panel design is shown in Figure 3.2-2. All of the user interface hardware (displays, switches, etc.), power supplies, fans, the card cage, and the 1272 NCO card have been installed in the unit. A 50 MHz oscillator source for the 1272 NCO card has also been included. With the exception of the phase shifter and lock detector circuits, all other circuits are completed. Preliminary open loop testing has been conducted on the synchronizer. This was done by replacing the EPROMs that contain the sine of the error function with EPROMs that contain a programmed sine wave. The sine wave is clocked into the loop filter and then to the NCO by means of a test counter circuit that is connected to the EPROM address lines. Using a 15 MHz quiescent frequency the carrier from the synchronizer swept back and forth

following the sine wave input to the loop filter. The next stage of testing will incorporate the demodulator and close the loop.

3.3 THE DEMODULATOR

The demodulator has both analog and digital circuitry. The front end is analog and comprised of off-the shelf RF circuit components. They have been selected and specified to meet power requirements in accordance with the input test signal, the sine and cosine from the carrier synchronizer, and with the inputs to the demodulator analog-to-digital converters . The test "received" signal is a composite signal constructed from the outputs of a 15 MHz frequency synthesizer and a NoiseCom white noise source (100 Hz to 500 MHz). The signal and noise are summed and amplified. This composite signal is then split, 3 ways, to supply the two quadrature mixers and an output test port from the demodulator. The NCO sine and cosine outputs are separately amplified using two-stage fixed and adjustable amplifiers. They are then mixed with the composite "received" signal. The mixer IF outputs are low-pass filtered at a 2 MHz bandwidth before entering the ADC circuits. The ADCs are multi-stage circuits and are the most complicated section of the demodulator. Both gain and DC offset must be achieved to drive the converters with the analog I and Q channel samples while maintaining amplifier stability. There are three op-amps in each ADC circuit (one for I and one for Q) to achieve the proper signal conditioning. The ADC's themselves, AD4098's, are clocked at 500 kHz, the same "symbol" clock that drives the carrier synchronizer. The 8-bit ADC outputs are sent to the carrier synchronizer and represent the I and Q samples that are used as addresses to the EPROM's. The construction of the demodulator will be completed by the end of July and.

3.4 TESTING

Once construction, checkout, and calibration of both the carrier synchronizer and the demodulator are completed, MPSK carrier tracking tests will begin. The theoretical work and simulation results on MPSK carrier tracking, completed under NAG5-1392 will be verified by conducting phase jitter measurements. The signal-to-noise ratio (SNR) can be varied by attenuating the noise source in the demodulator. An HP 5172A time and frequency analyzer will be used to conduct jitter measurements. Further the lock threshoids of 8 PSK and 16 PSK can be compared with those of the simulation results.

3.5 CONCLUSIONS

After the phase jitter and lock threshold testing has been completed, it will be possible to further explore the use of optimal MAP estimation in MPSK carrier tracking as discussed in Section 2 of this report. By replacing the synchronizer EPROM's, which contain the high SNR approximation to MAP estimation, with EPROM's that contain the optimal solution, it will be possible to study the effects on phase jitter and lock thresholds that using the current standard of the high SNR approximation has on 8 PSK and 16 PSK.

The entire system has been constructed with the idea that it can be used as an MPSK receiver with minimal engineering changes. Incorporating a phase shifter and lock detector with an external symbol synchronizer will complete the design of a fully functional MPSK receiver. This will be a valuable laboratory tool in the analysis of communications systems that utilize MPSK.

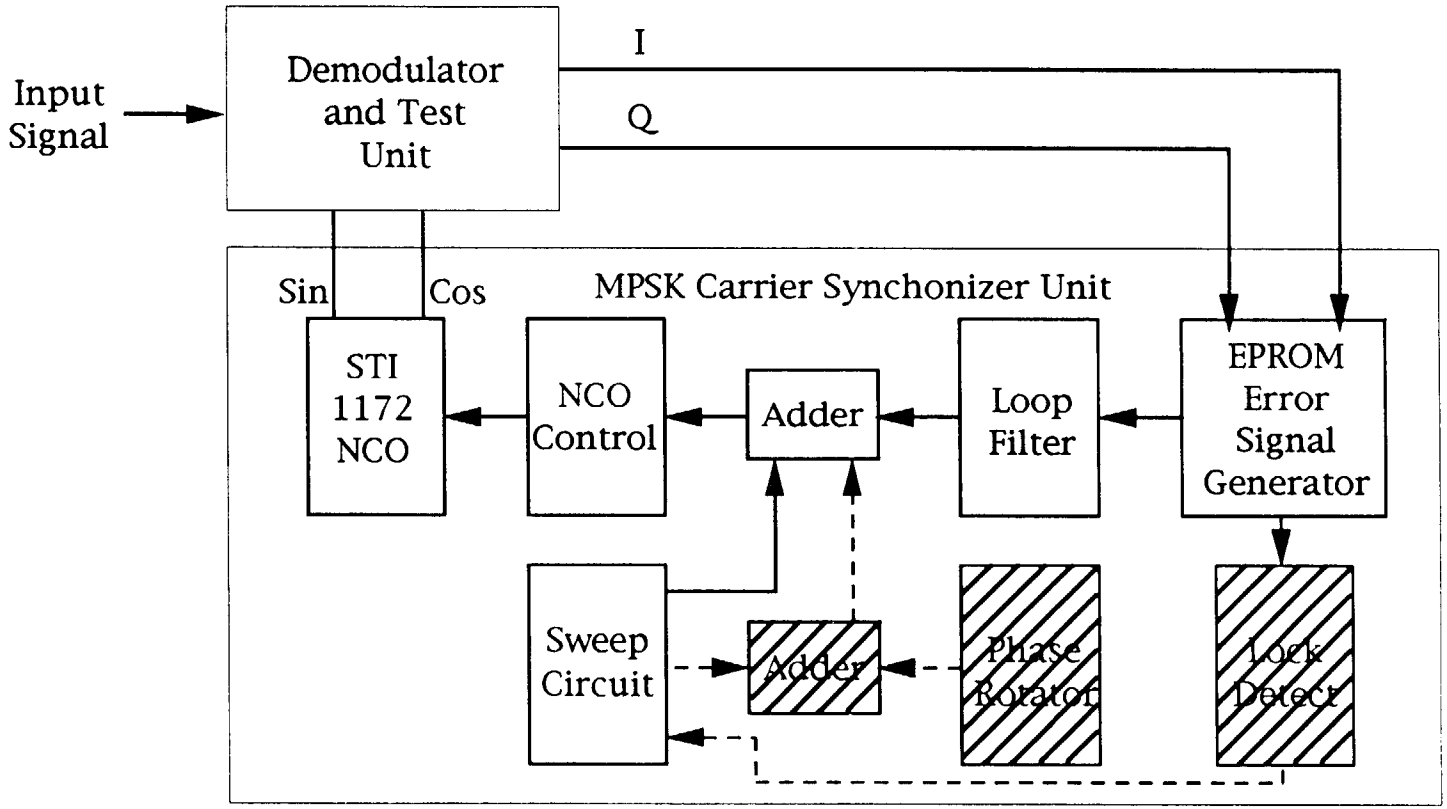

Note: For test purposes symbol timing is assumed.

Figure 3.1-1. The carrier tracking test system, emphasizing the carrier synchronization circuitry

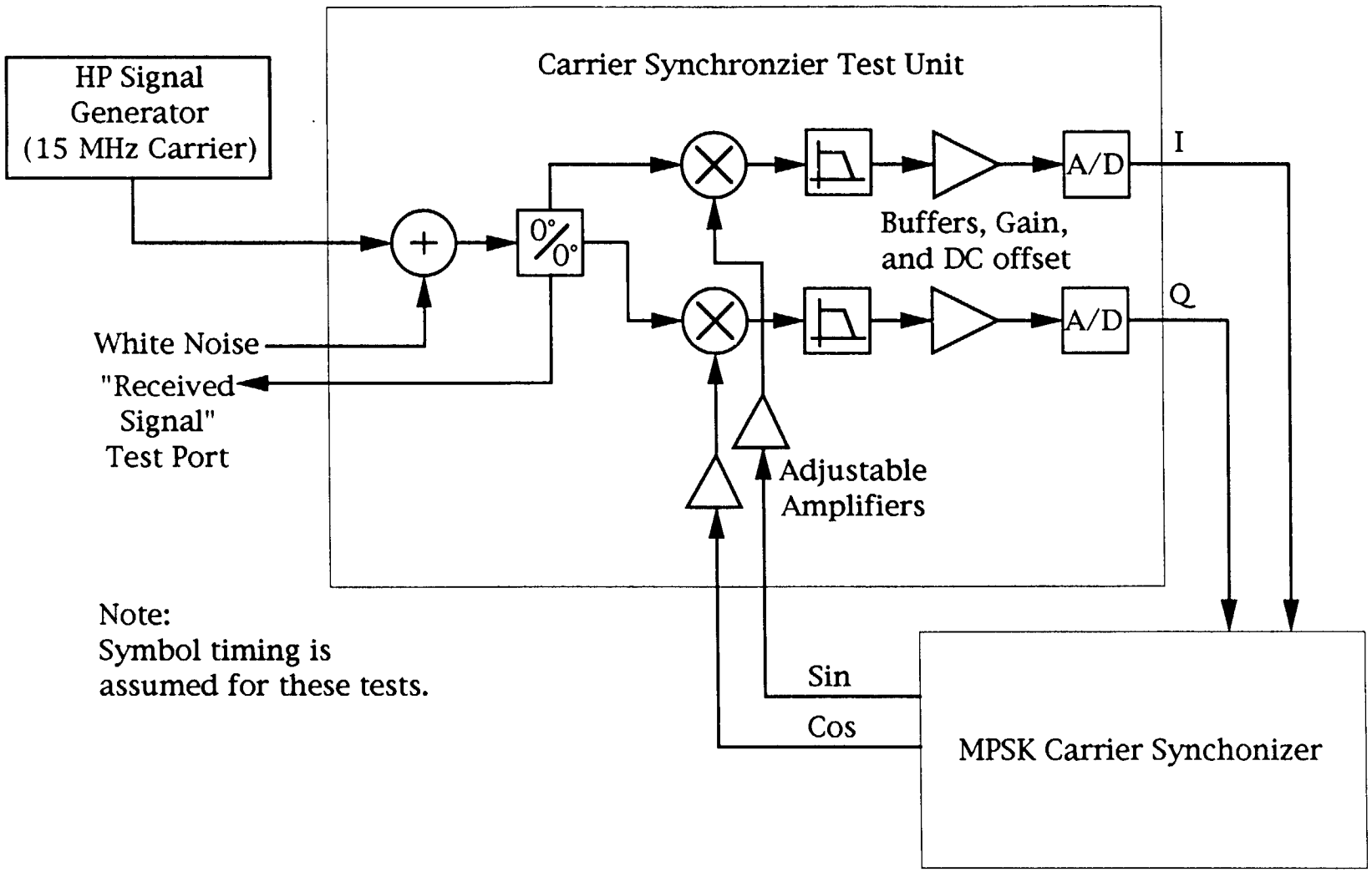

Figure 3.1-2. The carrier tracking test system, emphasizing the demodulation circuitry.

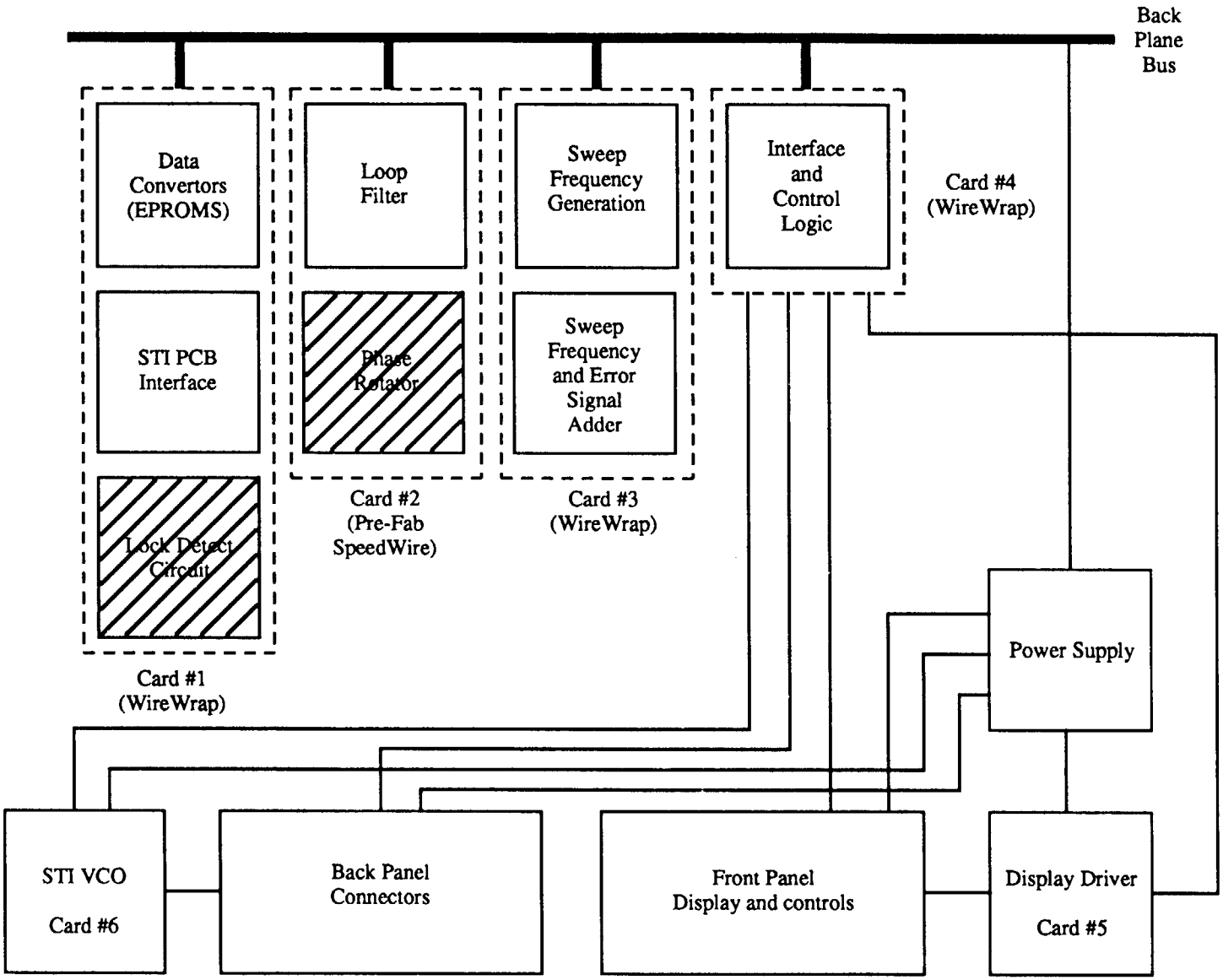

Figure 3.2-1. MPSK Carrier Synchronizer Block Diagram.

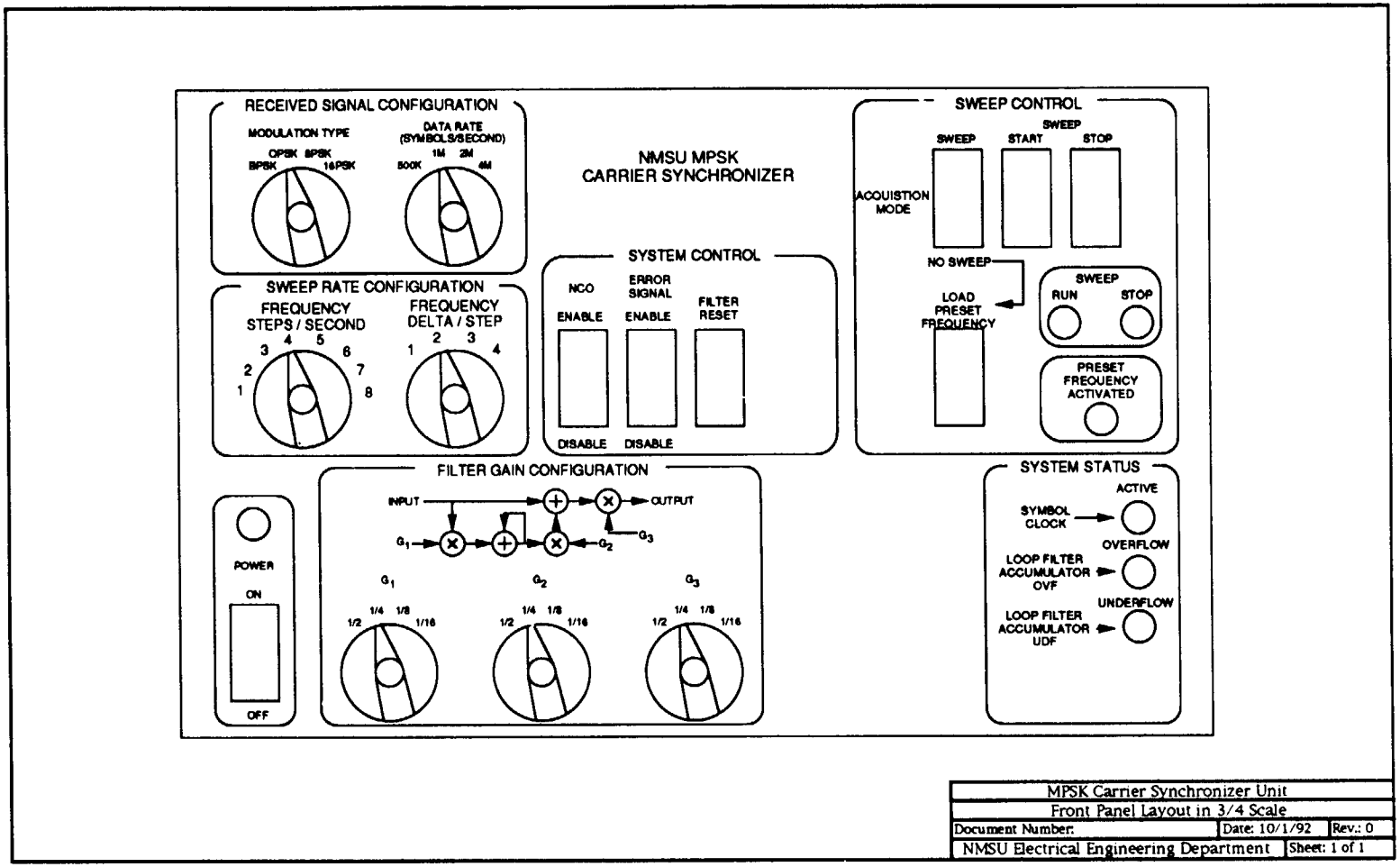

Figure 3.2-2. MPSK carrier synchronizer front panel artwork.

SECTION 4: THE EFFECTS OF RADIO FREQUENCY INTERFERENCE ON TRELLIS CODED MODULATION

4.1 OVERVIEW

Trellis coded modulation (TCM), pioneered by Ungerboeck [1, 2] has been cited as the modulation technique for the next generation of space communication systems. This being the case, the performance of TCM systems exposed to additive white Gaussian noise (AWGN) has been researched thoroughly. However, questions have surfaced concerning how well TCM systems will respond to radio frequency interference (RFI).

This paper presents results of simulations geared to measure the performance of TCM systems in radio-frequency (RF) co-channel interference and burst interference. The software package, Block Oriented Simulation Software (BOSS), was used to simulate (at rate 2/3) a 16 State TCM system with Viterbi decoding and a Pragmatic TCM system [4]. The performance of the systems is measured by their bit error rate (BER) as a function of signal to effective interference ratio.

Results show that when compared to the uncoded, quadrature phase shift keying (QPSK) system, TCM achieves a substantial coding gain when subjected to a mixture of AWGN and co-channel interference. It is a fact that BER performance of TCM systems degrades significantly as a result of burst interference. However, periodic convolutional interleavers (PCI) can recover some of the losses.

4.2 INTRODUCTION

It has been effectively argued that Trellis coded modulation (TCM) provides a variety of advantages for space communications [5 & 6]. In such an environment (bandlimited, power limited and possible low signal to noise ratio (SNR)), TCM provides coding gain, and error correction without an increase in bandwidth. The bit error rate performance of TCM systems in Additive White Gaussian Noise (AWGN) has been well documented theoretically and by simulations [1, 2, 3, 5, 6, & 9]. While trellis codes have been proven for Gaussian channels, their performance in non-Gaussian noise has been brought into question. In this project two cases of non Gaussian interference will be studied, co-channel interference and burst interference.

Co-channel interference is a typical source of degradation and has been the subject of some other investigations. For example, Losquadro et al published results on a study of RFI in DRS links and the impact on coding schemes used in that system [13]. Other theoretical works have examined M-ary PSK subjected to AWGN and RFI [7].

The second case to be studied is that in which the interfering signal occurs in bursts. It is already known that TCM performs poorly when the interference occurs in bursts [8]. A popular scheme used to combat burst errors is interleaving. In a paper published in 1971, G. D. Forney detailed the structure of the convolutional interleaver used to combat bursts on the channel [10]. A report published by Richer demonstrated improved performance with block interleaving for a Viterbi decoder subjected to burst interference [11]. Evaluations of how well communication systems work when subjected to various kinds of interference is an ongoing task. As new systems are developed, like TCM, they are put through the 'rings' to determine their limitations.

The Telemetry Center at New Mexico State University (NMSU) has developed a data-base of TCM systems and simulation results in BOSS. From the data base two systems, 16-State TCM and Pragmatic TCM, were selected for this study. The details of their design can be found in [5 & 6]. Both systems make use of an 8-PSK (phase shift keying) signal set and their co-ordinates are transmitted over 'I' and 'Q' channels (in-phase and quadrature). Use of such a signal set for simulations lessens the amount of memory used, and the sampling requirements for signals. The TCM systems were re-configured to include a RFI vector source (co-channel interference model) and their bit error rate (BER) performance tested.

Regardless of how the coded system is affected by various kinds of interference, it should be kept in mind that the value of coding is determined by comparing the performance of an uncoded system subjected to identical conditions.

4.3. CO-CHANNEL INTERFERENCE

To a user, co-channel interference is any unwanted signal energy within a frequency band of interest. The sources of such interference are many and varied but may be typified by signals from adjacent frequency bands. It is clear that whatever the source, such signals will cause degradation in the performance of communication systems.

In order to characterize the performance of TCM systems, the approach taken in this effort is to generate a parametric family of BER curves as a function signal to composite interference ratio. The total interfering power is the sum of AWGN and the RFI source in the channel. Each curve is classified based on the percent RFI energy content of the total interference. Comparisons are made with the corresponding uncoded QPSK system under the same conditions. For this purpose the systems were constructed in BOSS for simulations. In these BOSS systems signals are represented as vectors and thus create a demand for a RFI vector space model (see Figure 4.3-1).

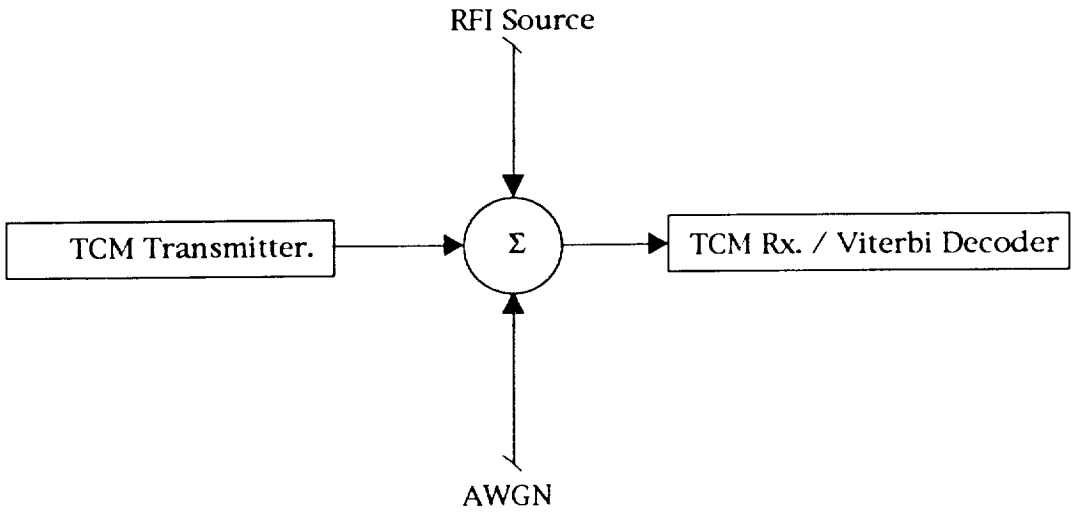

Figure 4.3-1 TCM System with RFI Model

4.4 RADIO FREQUENCY INTERFERENCE VECTOR MODEL

Figure 4.4-1 illustrates the vector space of a QPSK signal set. A vector space model of RFI may be described as follows for co-channel interference. The interfering signal is considered as a sinusoid with fixed amplitude and fixed frequency within the transmission bandwidth, $A*\sin[\ \omega_i t + \Theta(t)\ ]$. The phase is a random variable uniform from $-\pi$ to π.

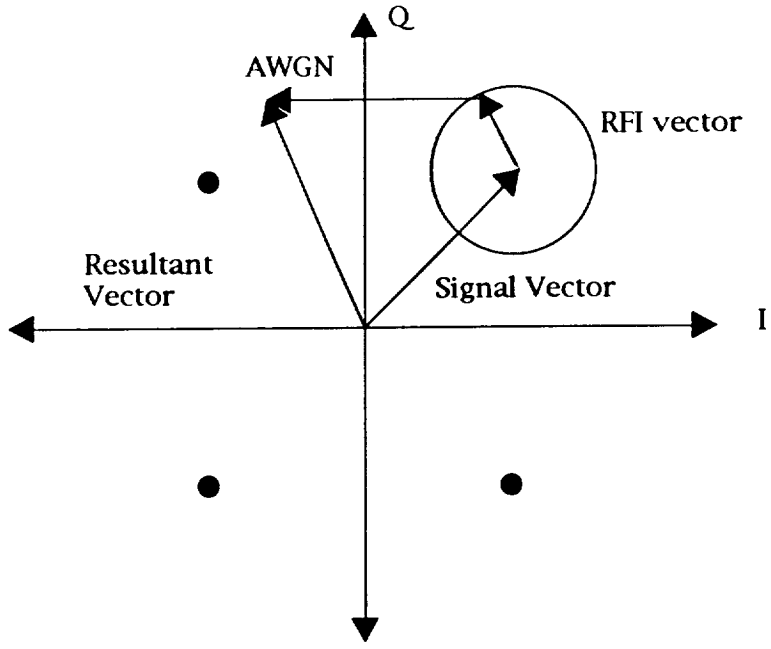

QPSK Signal Set

Figure 4.4-1 RFI Vector Model

The received signal is therefore the sum of the transmitted symbol, AWGN, and RFI. Correlation with reference signals $\sqrt{\frac{2}{T}}\cos[\,2\pi f_s t\,]$ and $\sqrt{\frac{2}{T}}\sin[\,2\pi f_s t\,]$, produces in-phase (I) and quadrature (Q) components of each term in the received signal. The correlator's response to the RFI produces an I-term

$$\frac{A}{T}\,\frac{\sin[\,2\pi (f_i - f_s)\,T + \Theta(t)\,] - \sin[\,\theta\,]}{2\pi (f_i - f_s)}$$

and a Q-term

$$\frac{A}{T}\,\frac{\cos[\,2\pi (f_i - f_s)\,T + \theta\,] - \sin[\,\theta\,]}{2\pi (f_i - f_s)}$$

Adding the sum of the square of the above terms gives the energy which is reduced to $A^2\,\mathrm{sinc}^2[(f_i - f_s)T]$. From this derivation it is justifiable to consider the effective amplitude of the interfering signal, the square root of the energy, as the magnitude of the above vector. Our model of the RFI

vector is therefore $A_{eff}\, e^{j\theta}$. Consequently the model results in a complex vector. The magnitude of this vector is a function only of the difference in frequency (between the interfering signal and the reference). θ is a random variable uniform from $-\pi$ to π. With this complex vector 'I' and 'Q' components are generated by extracting the real and imaginary parts.

4.5 GENERATING THE RFI MODEL IN BOSS

A block diagram of the BOSS modules used are show in Figure 4.5-1. The phase is derived from a random number generator whose output is uniform from $-\pi$ to π. The phase term is made complex and is then multiplied by, 'A_{eff}', the magnitude of the interfering vector.

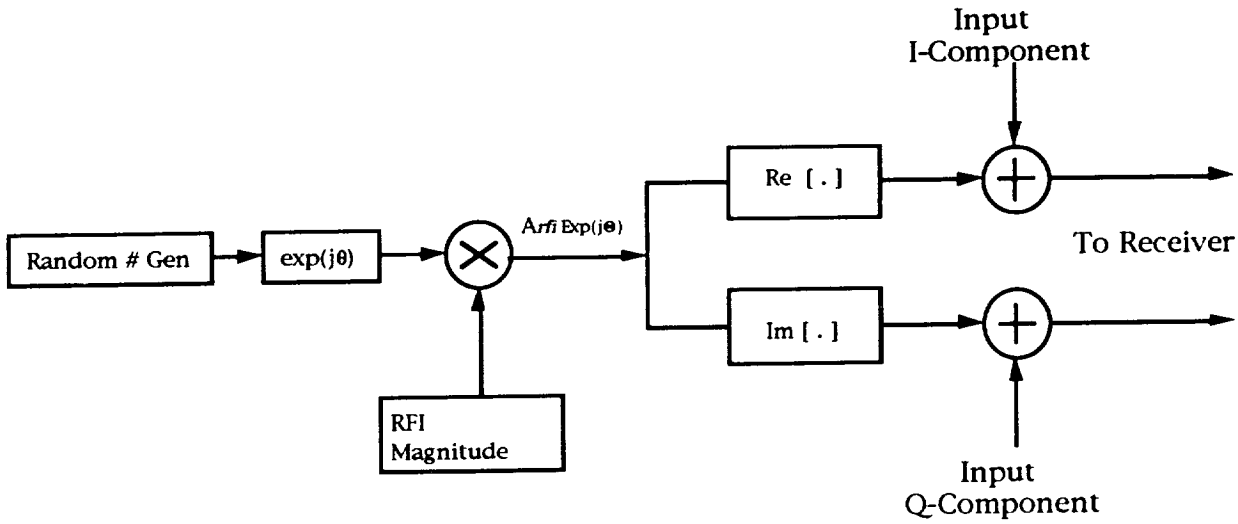

Figure 4.5-1 RFI Source Model

Outputs from the 'Real' and 'Imaginary' modules, I and Q respectively, are the additive interference to I and Q components of the message. With this new channel module inserted in the already built systems, their BER performances were measured. Plots of BER verses signal energy to noise ratio are shown in Figures 4.6-1, 4.6-2 and 4.6-3. The noise source is the sum of AWGN and RFI.

4.6 CO-CHANNEL RESULTS

Figures 4.6-1 to 4.6-3 show the parametric BER plots for the uncoded QPSK system and Trellis Coded 8-PSK systems. The TCM systems used are the 16-State system introduced by Ungerboeck [1 & 2], and the Pragmatic

TCM, more recently introduced by Viterbi [4]. Plots are shown for RFI comprising from zero to one hundred percent of the total interfering signal in increments of twenty five percent. It can be seen from the plots that there are significant coding gains relative to the uncoded case. As an example, at 25% RFI for a BER of 10^{-4} there is about 2 to 2.4 dB coding gain. However, there is an exception, the uncoded system responds better than the convolutional code when there is 100 % RFI. This result is due to typical limitations on the RFI energy. The magnitude of the RFI vector may not be sufficiently large to cause a bit error.

Comparing the two TCM systems, the 16 State machine performs better than the pragmatic system (0.5 dB difference at 50% RFI). This difference in performance is due to the uncoded outboard bit used in the pragmatic system. It is, however, well worth noting that the pragmatic system is not optimal but, provides about 1.7 dB of coding gain compared to uncoded QPSK.

4.7 BURST INTERFERENCE

Perhaps the most popular source of man-made burst interference is a pulsed radar transmitter. Lightening is a natural phenomena also known to introduce random burst interferences. Therefore, communication transmissions over these channels introduces bursts as well as additive white Gaussian noise to message signals. Assuming that the occurrence of bursts are ideally discernible, they are treated as erasures in the received data. Parameters of the bursts that are of interest to the communicator are its duration and arrival interval. Two models of bursts interference were looked at. The first case modeled the burst as periodic pulses with regular arrivals. In this case the burst can be varied to control the length 'B'

(number of symbols erased) and the period 'P_B' in which it repeats. For the

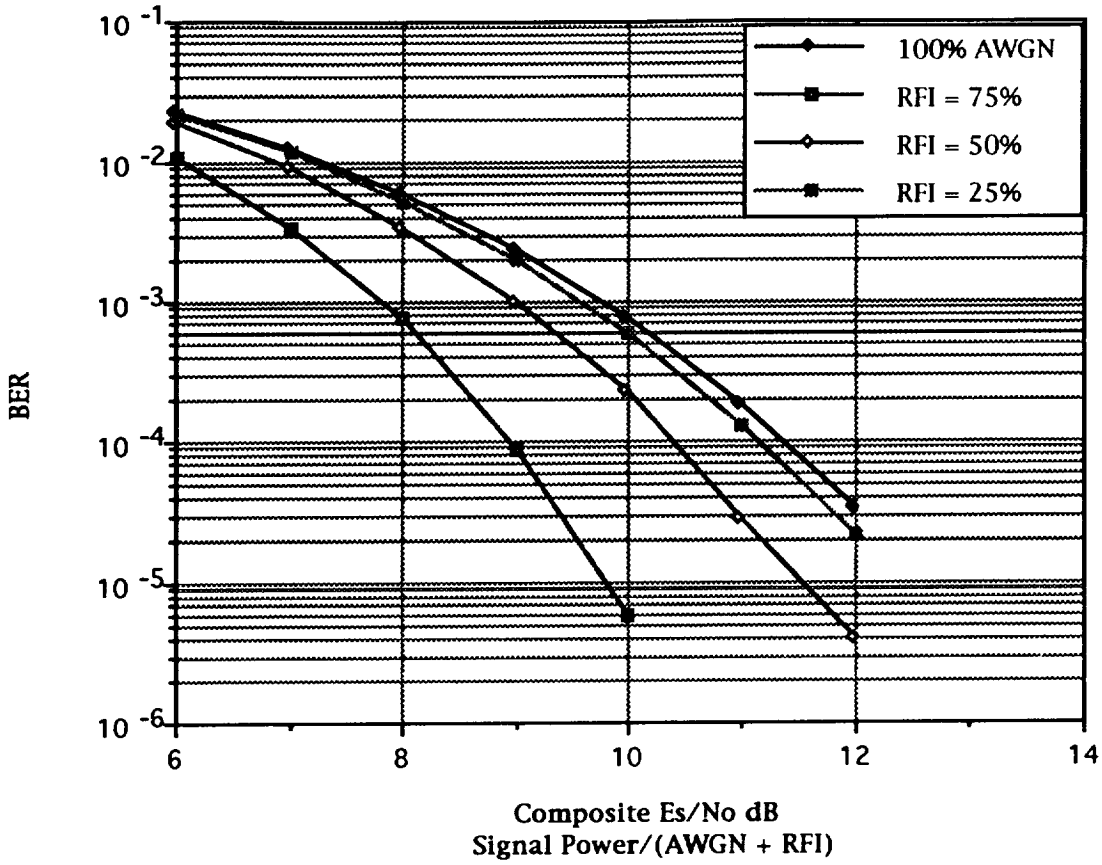

Figure 4.6-1 Bit Error Rate vs SNR for QPSK.

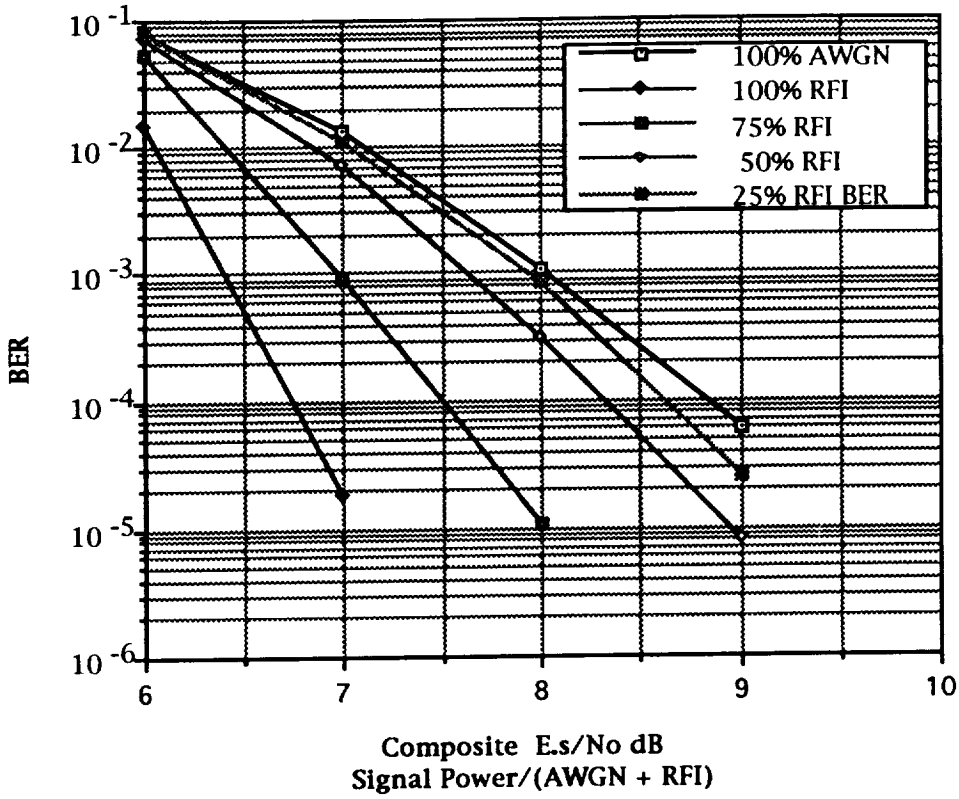

Figure 4.6-2 Bit Error Rate vs SNR for 16-State Convolutional Encoder.

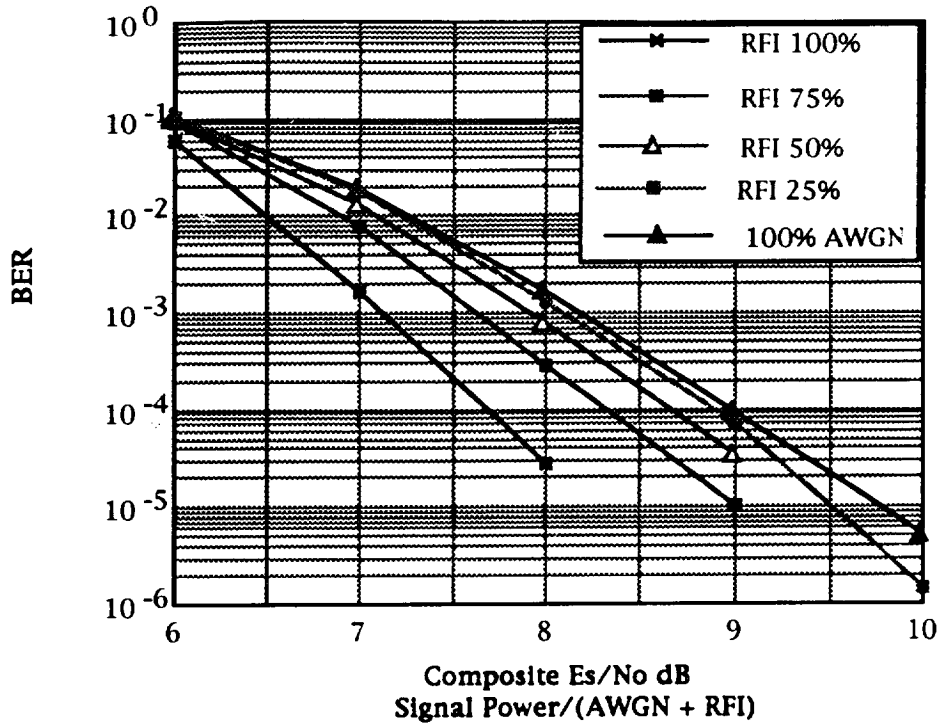

Figure 4.6-3. Bit Error Rate vs SNR fo Pragmatic System.

second case the occurrence of a burst was random and the inter-arrival time had a Poisson distribution. The parameter 'B' as before controls the length while λ controls the average arrival time. The general burst structure is shown in Figure 4.7-1.

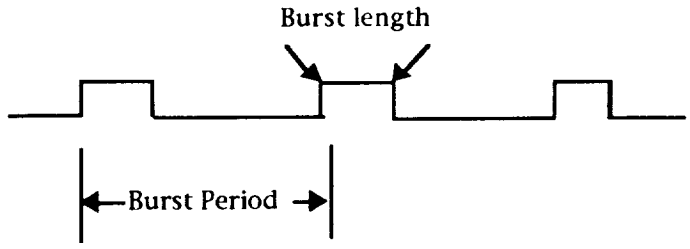

I 01010xxxxx010101101010xxxxx010101001010xxxxx01010.....

Q 11010xxxxx110101101111xxxxx110010110111xxxxx11001.....

x = Erased Symbols

Figure 4.7-1 Burst Parameters

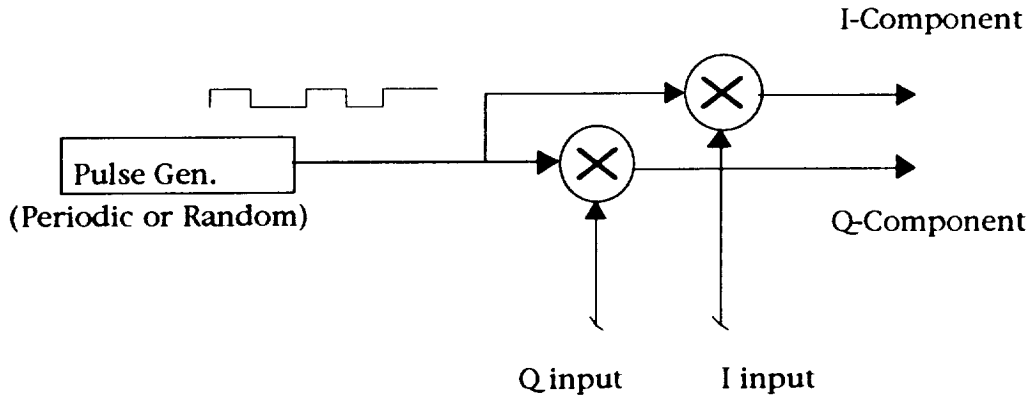

Figure 4.7-2 RFI Burst Model

BOSS modules were designed to generate both burst characteristics described above (see Figure 4.7-2). A pulse generator was used to produce the effects of recurring bursts. The pulse generator has output levels of zero and one. During the effected burst, the components of the signal vector are multiplied by zero or effectively erased. The rationale of designing the simulation in this fashion is as follows. True burst interference is of sufficient energy to render the information from the received signal vector essentially useless. This is the same effect as an erasure. Message symbols are erased when multiplied by the zero level of the pulse and this is done for the desired burst length. The burst interference sources were implemented with the TCM systems and BER were measured. During the occurrence of each burst 'B' symbols are erased. It is well known that convolutional codes responds poorly to these types of correlated errors [8]. Figures 4.7-3 and 4.7-4 show the performance curves both TCM systems with periodic bursts. Plots show, parametrically, the average number of incorrectly decoded output bits as a function of burst length at fixed signal-to-noise ratio. The degradation due to the burst is well illustrated by these plots. In low signal-to-noise ratios the bit errors are in excess of the number of erased symbols. However, as the SNR is increased the Viterbi decoder is able to correct erasures. This ability to correct erasures declines as the burst length increases. This error correction, even in the higher SNR, is an advantage compared to an uncoded QPSK system which offers no protection at all.

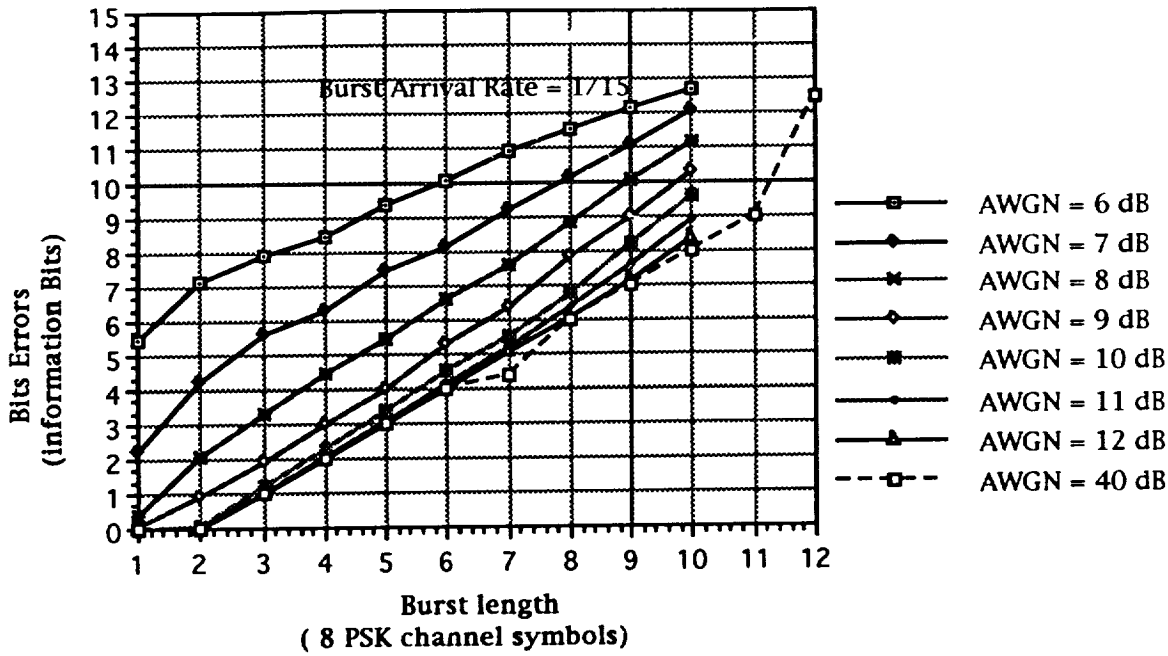

Figure 4.7-3. Bit Errors vs Burst Length for 16-State System.

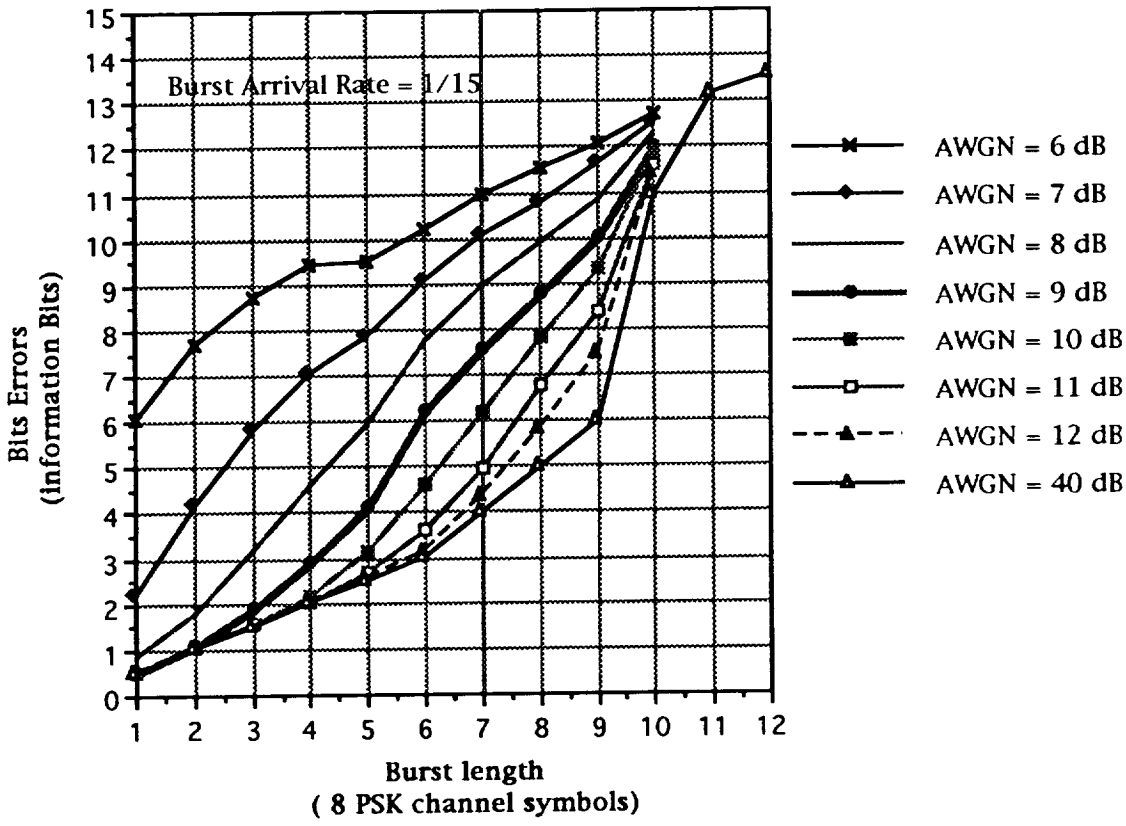

Figure 4.7-4. Bit error vs. Burst Length, Pragmatic System.

For the uncoded QPSK system the probability of a bit error (with AWGN & periodic burst) is given by

$$(1 - \delta)\cdot Q\left[\sqrt{\frac{2E_b}{N_0}}\right] + \frac{1}{2}\cdot\delta ,$$

where δ is the duty cycle of the burst. For high values of E_b/N_0 the error probability is dominated by the burst duty cycle. If the arrival of the burst is random with a Poisson distribution, the error probability is obtained as follows. Let λ be the average arrival rate of the burst. The probability of a single burst occurring in this time is given by

$$p = 1 - (1 - e^{-\lambda})^B ,$$

where B is the length of the burst. The δ term in the previous equation is replaced by the expression 'p', above, to give

$$(1 - p)\cdot Q\left[\sqrt{\frac{2E_b}{N_0}}\right] + \frac{1}{2}\cdot p.$$

Once the QPSK system is subjected to burst interference its BER performance is limited by the nature of the burst. No amount of reshuffling or spreading (interleaving) of the burst will help. For a 10% duty cycle burst the bit error probability for QPSK approaches 0.05 (independent of E_b/N_0). TCM systems, unlike QPSK, responds better when bursts are interleaved.

4.8 PERIODIC CONVOLUTIONAL INTERLEAVING

The periodic convolutional interleaver (PCI) used in this study was proposed by G. D. Forney. (See Figure 4.8-2). Convolutional interleavers offer some advantages over the more familiar block interleavers. Less memory storage, and shorter message delays are the major advantages of PCI over block interleaving. An interleaving example follows. Generally a communication system transmits sequential messages. If a burst is five symbols long, then each time a burst occurs five consecutive message symbols will be erased. As discussed previously, the Viterbi decoder will correct erasures provided that the interval between them is sufficiently long. The purpose of the interleaver is to scramble the transmitted

sequence so as to increase the distance between erased symbols at the receiver (see Figure 4.8-1).

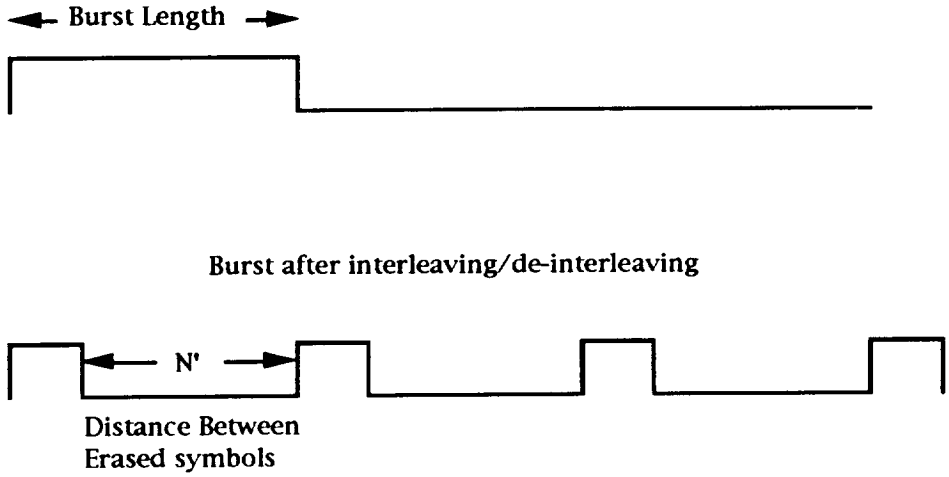

Figure 4.8-1 Interleaver/De-interleaver Response to Bursts

If the distance between erased symbols is sufficiently large the decoder is likely to perform much better than had the erasures remained clustered.

Figure 4.8-2 shows the basic structure of the convolutional interleaver and its output. The de-interleaver at the receiver re-orders the received symbols to their original positions. Each line in the interleaver/de-interleaver has shift registers used to delay the input symbols. The first and last lines of the interleaver have no delay. Interleaving is accomplished by the action of the synchronized commutator and the various delays introduced by registers. 'M' is the smallest multiple of shift registers on any line. The interleaver depth 'D' is the maximum burst length that can be tolerated. N' = D * M is the minimum distance between consecutive symbols. The distance between consecutive erased symbols is however D * M - 1. This is illustrated in Figure 4.8-2 which shows the interleaved channel input. If a burst occurs, it affects the column of the matrix where each element in a column is separated by D * M - 1.

In Figure 4.8-2 the interleaver shown has a depth of 5. Also M is equal to one; therefore, the distance between erased symbols is four. By increasing M, the number of shift registers, the distance between erasures is increased (so are the delays).

A PCI, with D = 5, of the structure described, was implemented in BOSS and tested with the TCM systems. Transmissions were subjected to different levels of AWGN as well as a periodic burst with a 10% duty cycle (five symbols erased every 50 symbols). Bit error rates were measured for different values of N' and plotted versus E_S/N_O. See Figures 4.9-1, 4.9-2, and 4.9-3.

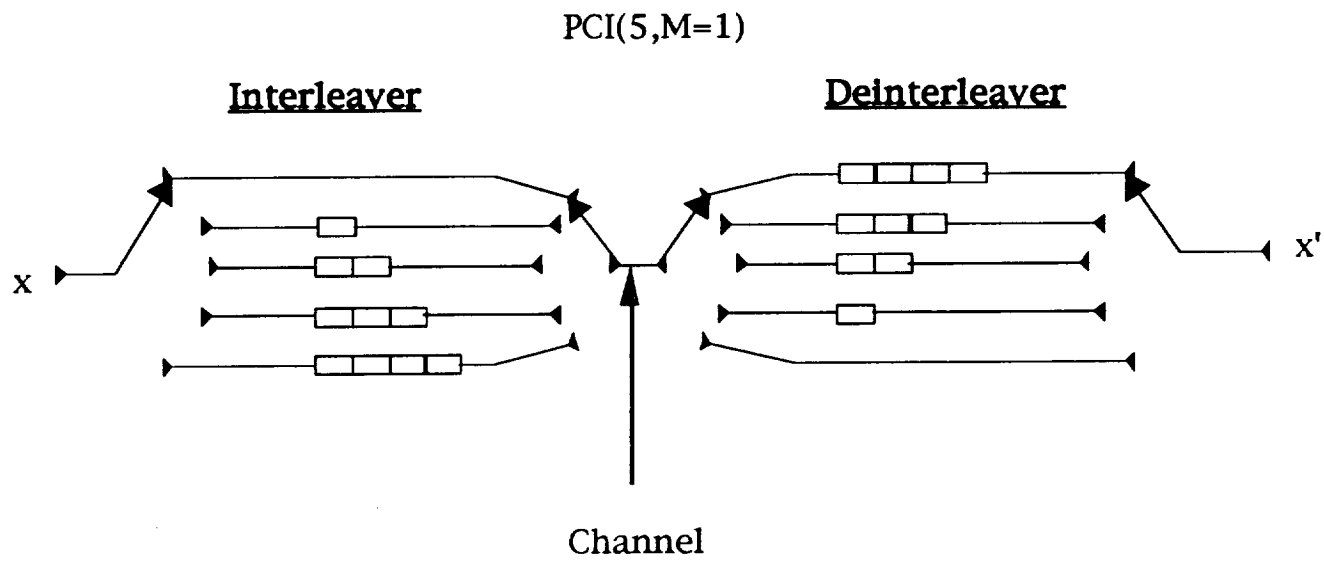

Channel Input

$$x_{i,n} := \text{if}(n + M\cdot(1 - i) - 1 \geq 0, (n + M\cdot(1 - i) - 1)\cdot D + i, -0)$$

$$x'' = \begin{bmatrix} 1 & 6 & 11 & 16 & 21 & 26 & 31 & 36 & 41 & 46 & 51 & 56 & 61 & 66 & 71 \\ 0 & 2 & 7 & 12 & 17 & 22 & 27 & 32 & 37 & 42 & 47 & 52 & 57 & 62 & 67 \\ 0 & 0 & 3 & 8 & 13 & 18 & 23 & 28 & 33 & 38 & 43 & 48 & 53 & 58 & 63 \\ 0 & 0 & 0 & 4 & 9 & 14 & 19 & 24 & 29 & 34 & 39 & 44 & 49 & 54 & 59 \\ 0 & 0 & 0 & 0 & 5 & 10 & 15 & 20 & 25 & 30 & 35 & 40 & 45 & 50 & 55 \end{bmatrix}$$

Figure 4.8-2 Periodic Convolutional Interleaver

As before the abscissa Es/No is due only to additive white Gaussian noise and does not include any power due to bursts. In this paper interleavers are labeled as PCI(D,M) where D is depth and M is the smallest multiple of shift registers on a line. This was done to track the complexity of the interleaver. The BER measurements are plotted parametrically on this basis.

4.9 BURST INTERFERENCE RESULTS

For a (5,50) burst (10% duty cycle) five of every symbols are erased. The maximum distance that can be achieved between consecutive erased symbols is therefore ten (10). That is to say the (5,50) burst is transformed into a (1,10) burst. The higher order of interleavers (greater than (PCI(5,2)) provides distances greater than 10 within a single burst. However, because the bursts repeat periodically this distance is not maintained and can even revert to the non-interleaved case. It is to be expected that the best BER performance is achieved when the distance between erasures is 10 symbols. The BER curves obtained indeed support this conclusion (see Figure 4.9-1). Results were also obtained for random occurrence of bursts. Periodic interleavers become vulnerable to variations in the arrival rate and length of bursts and therefore perform worst when subjected to random bursts. Results also show that higher order interleavers provided better improvements for random bursts when compared to performances in periodic bursts.

No amount of interleaving of the bursts recovered any losses for the Pragmatic TCM system. This result is due to the uncoded bit that is

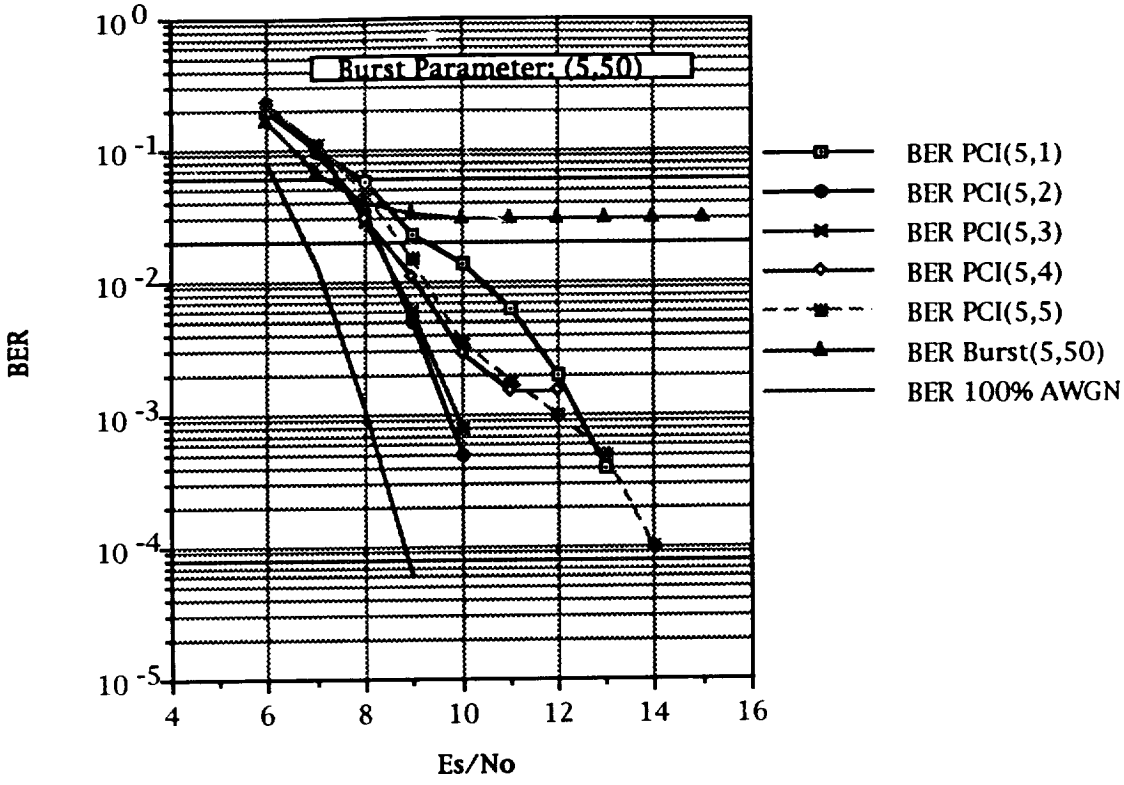

Figure 4.9-1. 16-State TCM BER Performance with 10% duty Cycle Burst and Periodic Convolutional Interleaving

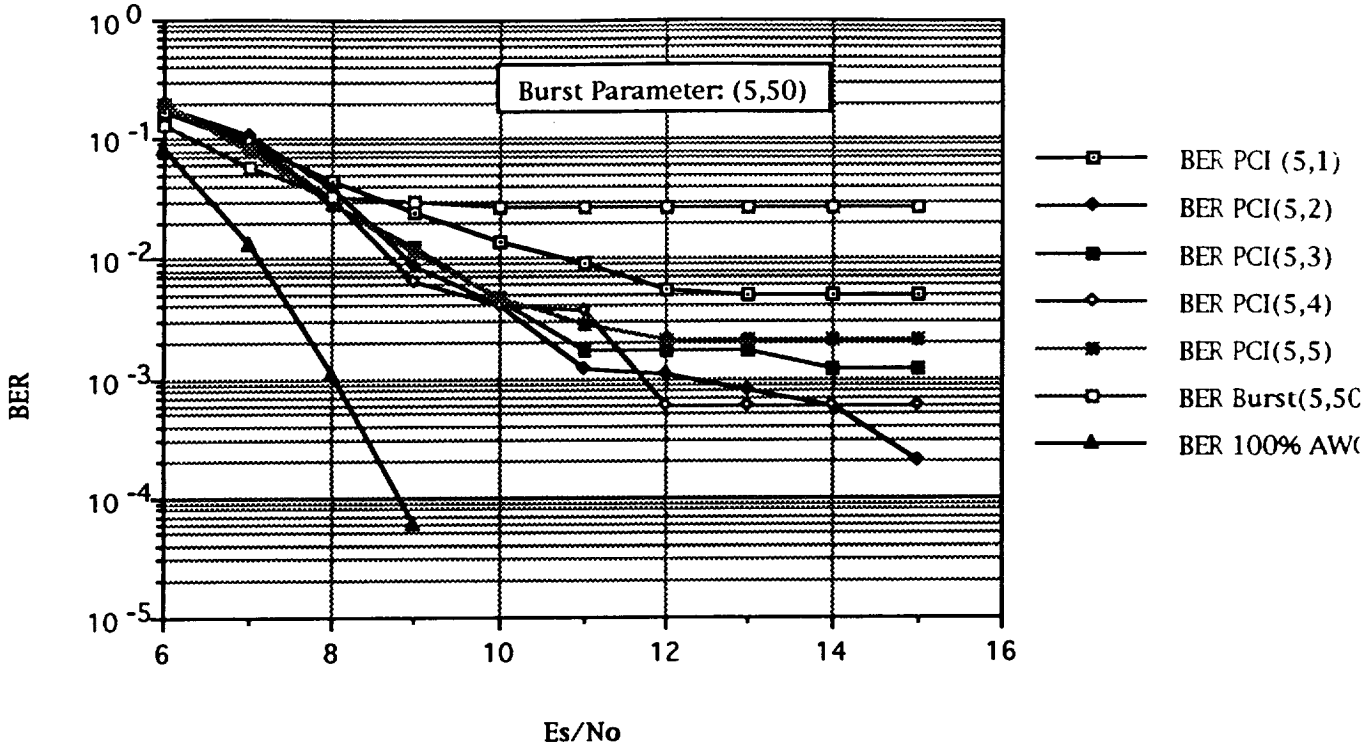

Figure 4.9-2. Bit Error Rate vs Es/N0 for Burst with Poisson Distributed Arrival Rate

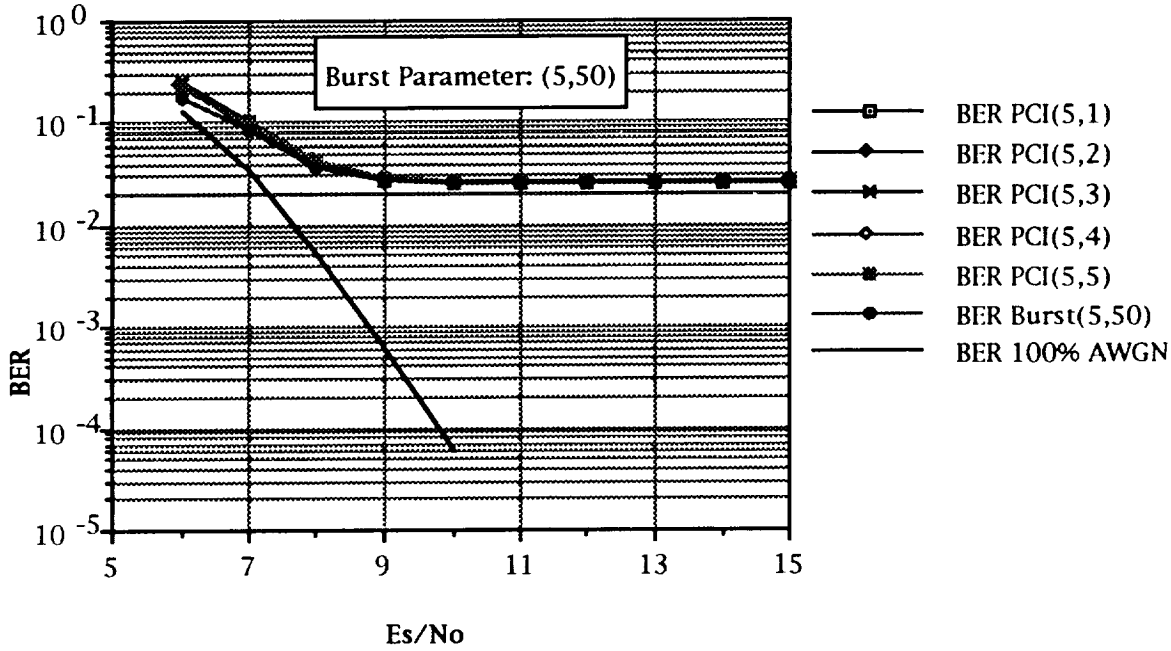

Figure 4.9-3 Pragmatic TCM BER

characteristic of the Pragmatic codes. The performance of the code is dominated by the outboard bits and interleaving does not provide any added protection (see Figure 4.9-3).

4.10 CONCLUSIONS

Trellis coded modulation (TCM) has been sighted as the modulation technique for the next generation of space communication systems 5 & 6. However, questions have surfaced concerning how well TCM systems will respond to radio frequency interference (RFI).

This paper presents results of simulations geared to measure the performance of TCM systems in radio frequency (RF) co-channel interference and burst interference. The software package, Block Oriented Simulation Software (BOSS), was used to simulate (at rate 2/3) a16 State TCM system with Viterbi decoding and a Pragmatic TCM system. The performance of the system is measured by their bit error rates (BER) as a function of signal to effective interference ratio.

Results show that when compared to the uncoded, quadrature phase shift keying (QPSK) system, TCM achieves a substantial coding gain when subjected to a mixture of AWGN and co-channel interference. This coding gain is in fact comparable to gains obtained with strictly Gaussian noise. It is a known fact that BER performance of TCM systems degrades significantly as a result of burst interference. However, periodic convolutional interleavers (PCI) can recover some of the losses. Interleaving is unsuccessful in recovering any losses when Pragmatic TCM systems are subjected to burst interferences. This result is due to the uncoded outboard bits.

It can be stated that, under practical conditions, a properly designed Trellis Coded Modulation system will out-perform an uncoded QPSK system in environments subjected to both Gaussian and co-channel interference, and burst interference.

4.11 REFERENCES

1. Ungerboeck, Gottfried, "Trellis-coded Modulation with Redundant Signal Sets, Part I: Introduction," IEEE Communications Magazine , Vol. 25, No. 2, pp. 5 - 11, February 1987.

2. Ungerboeck, Gottfried, "Trellis-coded Modulation with Redundant Signal Sets, Part II: State of the Art," IEEE Communications Magazine , Vol. 25, No. 2, pp. 12 - 21, February 1987.

3. Viterbi, A. J. , "Convolutional Codes and their Performance in Communicational Systems," IEEE Transactions on Communication Technology , Vol. CT-19, pp. 751 - 771, October 1971

4. Viterbi, Andrew J. , Jack K. Wolf, Erhraim Zehavi, Roberto Padovani, "A Pragmatic Approach to Trellis-Coded Modulation," IEEE Communications Magazine, Vol. 27, No. 7, pp. 11 - 19, July 1989.

5. Ross, M. D., Carden, F., Osborne, W. P., "Pragmatic Trellis Coded Modulation: A Simulation Using 24-Sector Quantized 8-PSK", Center for Telemetry Research, New Mexico State University, Las Cruces, NM

6. Carden, F., Ross, M. D., "64-State TCM for Spectrally Efficient Space Communications", Center for Telemetry Research, New Mexico State University, Las Cruces, NM

7. Shimbo, O., Fang, R., "Effects of Co-channel interference and Gaussian Noise in M-ary CPSK Systems", PP 233-244, from Interference Analysis of Communication Systems, IEEE Press, edited by Peter Stavroulakis, 1980

8. Clark, G. C., Cain, J. B., Error-Correction Coding for Digital Communications, Plenum Press, New York, 1981

9. Sklar, B., Digital Communications Fundamentals and Applications, Prentice Hall, Englewood Cliffs, New Jersey 1988

10. Forney, G. D., "Burst-Correcting Codes for the Classic Bursty Channel", IEEE Trans. Commun., Com-19, 772 - 781, Oct. 1971

11. Richer, I., "A Simple Interleaver for Use with Viterbi Decoding", IEEE Transaction on Communication, Vol. Com-26, No. 3, PP 406 - 408, March 1978

12. Berman, T., Freeman, J., Kaplan, T., " An Analytic Analysis of A Concatenated Reed-Solomon/ Viterbi Coding System Both with and without RS interleaving", Stanford Telecomm, 7501 Forbes Blvd. SeaBrook, MD 20706

13. Losquadro Giacinto, Michel Philippe, Elia Michele, Visintin Monica, " Impact of RFI Detection in DRS Links on the Performance of Coding Schemes",

SECTION 5. CONCATENATED TRELLIS-CODED MODULATION

5.1 INTRODUCTION

Concatenated systems combining the error correcting power of trellis code and Reed-Solomon (RS) codes have been used to achieve error rates between 10^{-10} and 10^{-20} on satelite communications links [1]. Typically such systems use binary or quaternary signalling, with an industry standard binary convolutional codes. The need for spectral efficiency has motivated consideration of of non-binary signalling with Ungerboeck [2,3] codes or the Pragmatic standard recently proposed by Viterbi [4]. In this paper we investigate the use of 8-PSK trellis-coded modulation (TCM) in a concatenated system. The outer code will be the (255,233) RS code, as this is the standard for current systems. This investigation concentrates on the effect of substituting TCM for the currently used binary inner code.

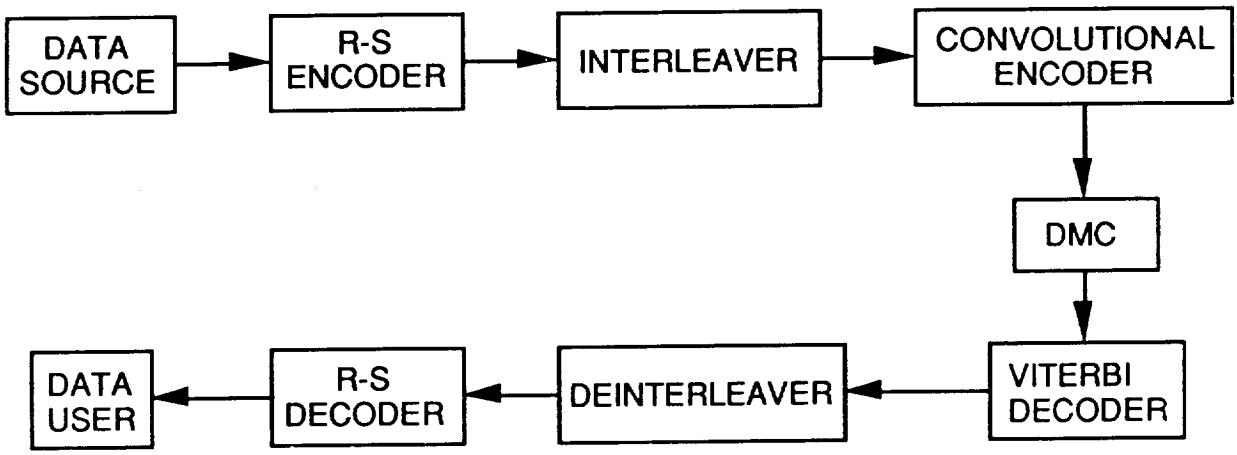

Figure 5.1-1. Concatenated Code System

A concatenated system is shown in figure 5.1-1. User data is first encoded by the RS Block encoder. The RS code symbols are then interleaved and convolutionally encoded. At the receiving end of the channel, modulated signals are decoded using the Viterbi algorithm, preferably with soft decisions. The output from the Viterbi decoder is then deinterleaved and RS decoded, recovering the user data. The RS code block consists of 255 symbols, a symbol being a block of 8-bits. An error in one or more of the eight bits of a given symbol results in a symbol error. The RS block code can correct up to 11 symbol errors.

The purpose of the interleaver is to aleviate the effect of burst noise during transmission. Given the structure of the RS code, we can see what the proper operation of the interleaver should be. Since a single bit error

in an RS code symbol counts as a symbol error, additional bit errors in the same symbol cause no further damage. An interleaver-deinterleaver operation which redistributes bit errors among multiple symbols in the same block will degrade, not improve, the performance of the system. Therefore, the interleaver should be designed to reduce the correlation between *symbol* errors, and to redistribute clustered symbol errors among several RS blocks. This fact will be important in the forgoing analysis.

Needless to say, it is not practical to measure bit error rates between 10^{-10} and 10^{-20} by computer simulation. When the concatenated system is operating in this range, the Viterbi decoder will be operating at a bit error rate between 10^{-3} and 10^{-5}. Therefore, it is feasible to characterize the Viterbi decoder output using simulations, and then algebraicly determine the resulting probability of error for the RS code. Such an approach has been used to predict the performance of concatenated systems with binary signalling [5], here we extend the technique to concatenated systems using TCM.

5.2 CHARACTERIZATION OF THE VITERBI DECODER OUTPUT

The approach used in [5] suggests that the output of the Viterbi decoder be modelled as a two-state first-order Markov process. The process, illustrated by the state diagram of figure 5.2-1, consists of a burst state, in which the probability of error is very high, and a clear state, in which the probability of error is very low. The process is characterized by the probabilities of transition from either state to the other. The transitional probabilities reflect the intercorrelation between errors in the Viterbi decoder output.

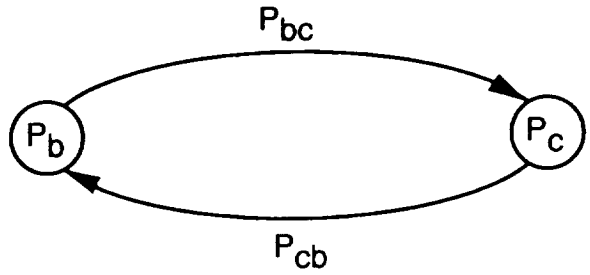

Figure 5.2-1. State Diagram for Markov Process Model

The Markov process is completely specefied by four parameters:

P_{1b} = probability of error when in burst state (5.2-1)

P_{1c} = probability of error when in clear state (5.2-2)

P_{bc} = probability of transition to clear state, when in burst state (5.2-3)

P_{cb} = probability of transition to burst state, when in clear state. (5.2-4)

From these four, additional useful parameters may be derived:

$P_{0b} = 1-P_{1b}$, the probability of non-error, when in burst state (5.2-5)

$P_{0c} = 1-P_{1c}$, the probability of non-error, when in clear state (5.2-6)

$P_{bb} = 1-P_{bc}$, the probability of remaining in burst state (5.2-7)

$P_{cc} = 1-P_{cb}$, the probability of remaining in clear state (5.2-8)

$P_b = \frac{P_{cb}}{P_{cb}+P_{bc}}$, the probability that the process will be in the burst state at any given time (5.2-9)

$P_c = \frac{P_{bc}}{P_{cb}+P_{bc}}$, the probability that the process will be in the clear state at any given time. (5.2-10)

To determine these parameters, which depend on channel signal-to-noise ratio, it is necessary to observe statistics of bit error patterns in the Viterbi decoder output. We define the following observable characteristics:

P_1 = the probability of a single bit error (5.2-11)

P_{11} = the probability of two consecutive bit errors (5.2-12)

P_{111} = the probability of three consecutive bit errors (5.2-13)

P_{101} = the probability of a bit-error, a (5.2-14)

non-bit-error, and a bit-error, in succession.

The observable characteristics are algebraicly related to the process parameters as follows:

$$P_1 = P_b P_{1b} + P_c P_{1c} \tag{5.2-16}$$

$$P_{11} = P_b P_{1b} P_{bb} P_{1b} + P_b P_{1b} P_{bc} P_{1c} + P_c P_{1c} P_{cb} P_{1b} + P_c P_{1c} P_{cc} P_{1c} \tag{5.2-17}$$

$$P_{111} = P_b P_{1b} P_{bb} P_{1b} P_{bb} P_{1b} + P_b P_{1b} P_{bc} P_{1c} P_{cb} P_{1b} + \ldots + P_c P_{1c} P_{cc} P_{1c} P_{cc} P_{1c} \tag{5.2-18}$$

$$P_{101} = P_b P_{1b} P_{bb} P_{0b} P_{bb} P_{1b} + P_b P_{1b} P_{bc} P_{0c} P_{cb} P_{1b} + \ldots + P_c P_{1c} P_{cc} P_{0c} P_{cc} P_{1c} \tag{5.2-19}$$

The expressions for P_{11} and P_{101} are similar to equations (5.2-16) and (5.2-17), except that they consist of eight terms of eight factors each.

If the two-state process is a valid model of the Viterbi decoder output, then the expressions for P_1, P_{11}, P_{111} and P_{101} (5.2-16 through 5.2-19) are four equations from which the four unknowns P1b, P1c, Pbc, and P_{cb} may be determined. The system is nonlinear, and there will in fact be two solutions, one of which exactly reverses the roles of the burst state and the clear state. Also, if $P_{bc} = P_{cc}$ and $P_{cb} = P_{bb}$, or if $P_{1b} = P_{1c}$, the model will generate a process in which bit errors are independent, and the solution will not be unique.

Given a set of numbers P_1, P_{11}, P_{111} and P_{101} not actually generated by the two-state process, a real solution may or may not exist. The algebraic solution of the system (5.2-16) through (5.2-19) is an exceedingly difficult exercise, and a reasonable approach to finding the model parameters is to use a numerical search to find the process parameters which match the observed characteristics. This approach was used to determine the parameters which charaterize the output of a TCM decoder.

5.3. CALCULATION OF THE PROBABILITY OF SYMBOL ERROR

Given the parameters of the Markov process, it is possible to calculate P(B), the probability that the process will be in the burst state B times during a symbol conisting of $K \geq 3$ bits. A symbol error is defined to

be the event that one or more of the bits of the symbol are in error. Therefore, the probability of symbol error is given by

$$P_S = \sum_{B=0}^{K} \left(1 - P_{0b}^{B} P_{0c}^{K-B}\right) \tag{5.3-1}$$

P(B) is found by considering the K-bit symbol to be divided into segments of consecutive bits in burst state or in clear state. If we let R_b be the number of segments in burst state, and R_c be the number of segments in clear state, then it is clear that $0 \leq Rb \leq B$ and $R_c = R_b - 1$, Rb or Rb + 1. Now,

$$P(B,R_b) = P(B,R_c=R_{b-1}) + P(B,R_c=R_b) + P(B,R_c=R_{b+1}) \tag{5.3-2}$$

$$P(B,R_c=R_b-1) \tag{5.3-3}$$

$$= \binom{B-1}{R_b-1}\binom{K-B-1}{R_c-1} P_b P_{cb}^{R_b-1} P_{bc}^{R_c} P_{bb}^{B-R_b} P_{cc}^{K-B-R_c}$$

$$P(B,R_b=R_c) \tag{5.3-4}$$

$$= \binom{B-1}{R_b-1}\binom{K-B-1}{R_c-1} P_b P_{cb}^{R_b-1} P_{bc}^{R_c} P_{bb}^{B-R_b} P_{cc}^{K-B-R_c}$$

$$+ \binom{B-1}{R_b-1}\binom{K-B-1}{R_c-1} P_c P_{cb}^{R_b} P_{bc}^{R_c-1} P_{bb}^{B-R_b} P_{cc}^{K-B-R_c}$$

$$P(B,R_b+1) \tag{5.3-5}$$

$$= \binom{K-1}{R_b-1}\binom{K-1}{R_c-1} P_c P_{cb}^{R_b} P_{bc}^{R_c-1} P_{bb}^{B-R_b} P_{cc}^{K-B-R_c}$$

The reasoning behind this is as follows. The combinatorial

$\binom{B-1}{R_b-1}$ is the number of ways that B periods in the burst state can be divided among R_b segments in burst state, and likewise $\binom{K-B-1}{R_c-1}$ is the number of ways that K-B periods in clear state can be divided among R_c segments in clear state. Every segment except the first segment begins with a transition, hence the factor P_{cb} or P_{bc} is used. The first segment begins with P_b or P_c. The remaining K periods must be non-transitions, hence P_{bb} or P_{cc}. Equations (5.3-1) through (5.3-5) are valid for $1 \leq B < K$, $R_b \geq 1$ and $R_c \geq 1$. If R_b=0 then B=0 and if R_c=0, B=K.

$$P(B=0) = P_c P_{cc}^{K-1} \tag{5.3-6}$$

$$P(B=K) = P_b P_{bb}^{K-1} \tag{5.3-7}$$

For 0<B<K:

$$P(B) = \sum_{R_b=1}^{K-1} P(B,R_b) \tag{5.3-8}$$

Where $P(B,R_b)$ is as specified by equations (5.3-1) through (5.3-5). Once P(B) is calculated using equation (5.3-8), the probability of symbol error is calculated using equation (5.3-1).

5.4. CALCULATION OF THE REED-SOLOMON BLOCK ERROR PROBABILITY

The (255,233) Reed-Solomon code consists of a block of 255 symbols of 8-bits each. Up to 11 symbol errors are correctable therefore, the probability of Block error is given by

$$P_e = 1 - \sum_{i=0}^{11} \binom{255}{i} P_s^i (1-P_s)^{255-i} \tag{5.4-1}$$

For completely independent bit errors:

$$P_s = 1 - P_1^8 \tag{5.4-2}$$

For bit errors described by the model of section II, P_S is calculated as described in section III, using K=8.

If the RS codebits are transmitted using a rate 2/3 8-PSK Ungerboeck code, each state transition of the Markov process must correspond to a period of operation of the trellis code, which corresonds to two decoded bits. Therefore, we introduce the term Viterbi decoded symbol to refer to a pair of bits which are decoded in one stage of the Viterbi decoder trellis, and a RS code symbol then consists of four Viterbi decoded symbols. In determining the parameters from the Markov process model, a Viterbi decoded symbol is conidered to be in error if either of its two constituent bits are in error, and this probability becomes the statistic P_1. Likewise, P_{11} denotes the probability of two consecutive Viterbi decoded symbol errors, and P_{111} denotes the probability of three such errors. The parameters of the Markov process are then evaluated using the method of section II, and P_S is evaluated as described in section III, using K=4. The validity of equation (5.4-1) depends on the independence of RS code symbol errors, which is effected by the interleaver designed to interleave blocks of four 8-PSK symbols.

5.5. RESULTS

Simulations were written in the C programming language to determine the probability of all patterns of errors in four consecutive Viterbi decoded symbols. The results for the 16-state Ungerboeck code are complete. The results for the pragmatic code and the 64-state Ungerboeck code are in progress. These results were used to calculate the probability of a block error in the Reed-Solomon code, which is plotted in figure 5.5-1.

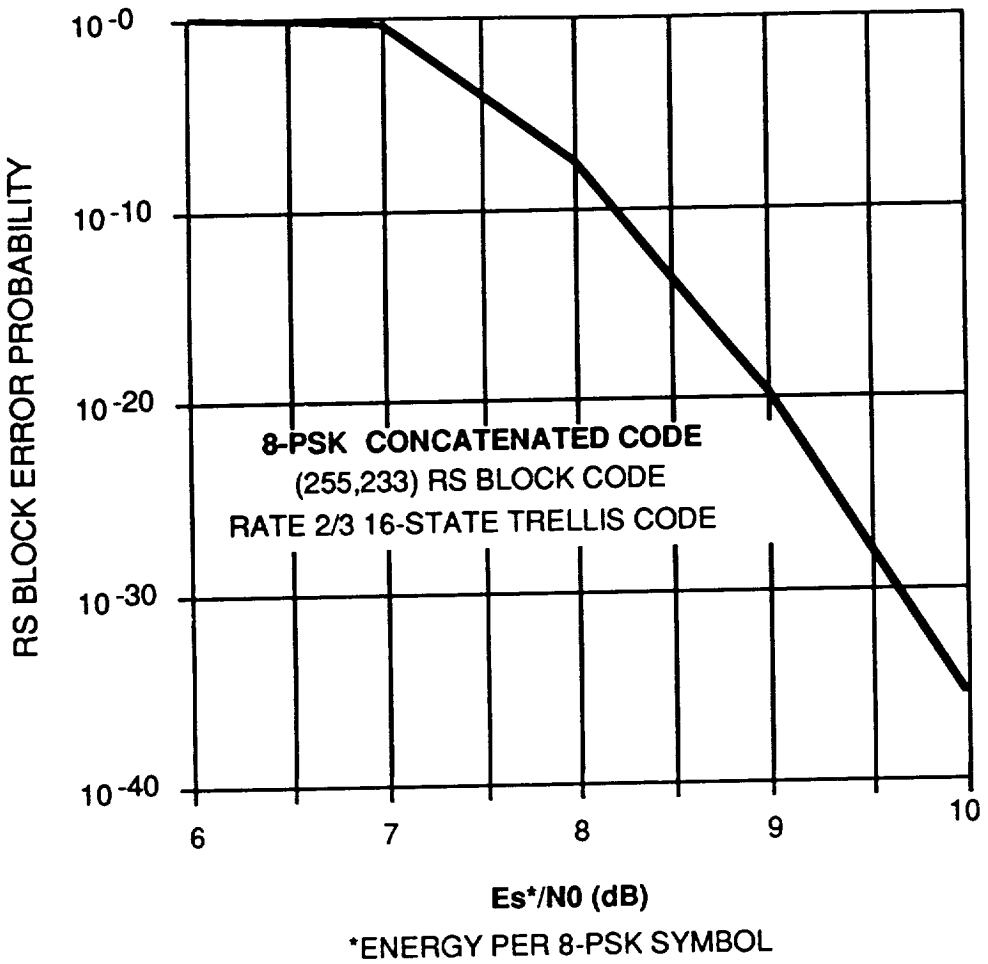

Figure 5.5-1. RS Block Error Probability for Concatenayed System

5.6 REFERENCES

[1] Forney, G. D., Jr., Concatenated Codes, MIT Press, Cambridge, Mass., 1966

[2] Ungerboeck, Gottfried, "Trellis Coded Modulation with Redundant Signal Sets, Part I: Introduction," IEEE Communications Magazine, Vol. 25, No. 2, pp. 5-11, February 1987.

[3] Ungerboeck, Gottfried, "Trellis Coded Modulation with Redundant Signal Sets, Part II: State of the Art," IEEE Communications Magazine, Vol. 25, No. 2, pp. 12-21, February 1987.

[4] Viterbi, Andrew J., Jack K. Wolf, Ephraim Zehavi, Roberto Padovani, "A Pragmatic Approach to Trellis-Coded Modulation," IEEE Communications Magazine, Vol 27, No. 7, pp. 11-19, July 1989.

[5] Miller, R.L., L. J. Deutsch, and S. J. Butman, "On the Error Statistics of Viterbi Decoding and the Performance of Concatenated Codes", JPL Publication 82-76, Jet Propulsion Laboratory, Pasadena, CA, Sept. 1, 1981.